

# USING MULTIWAVELENGTH OBSERVATIONS TO DETERMINE THE BLACK HOLE MASS AND ACCRETION RATE IN THE TYPE 1 SEYFERT GALAXY NGC 5548

JAMES CHIANG<sup>1,2</sup>

NASA/GSFC, Code 661, Greenbelt MD 20771

OMER BLAES

Department of Physics, University of California, Santa Barbara CA 93106-9530

*Accepted for publication in ApJ*

## ABSTRACT

We model the spectral energy distribution of the type 1 Seyfert galaxy NGC 5548, fitting data from simultaneous optical, UV, and X-ray monitoring observations. We assume a geometry consisting of a hot central Comptonizing region surrounded by a thin accretion disk. The properties of the disk and the hot central region are determined by the feedback occurring between the hot Comptonizing region and thermal reprocessing in the disk that, along with viscous dissipation, provides the seed photons for the Comptonization process. The constraints imposed upon this model by the multiwavelength data allow us to derive limits on the central black hole mass,  $M \lesssim 2 \times 10^7 M_\odot$ , the accretion rate,  $\dot{M} \lesssim 2.5 \times 10^5 M_\odot \text{yr}^{-1}/M$ , and the radius of the transition region between the thin outer disk and the geometrically thick, hot inner region,  $\sim 2\text{--}5 \times 10^{14}$  cm.

*Subject headings:* galaxies: active — galaxies: individual (NGC 5548) — galaxies: Seyfert — X-rays: galaxies

## 1. INTRODUCTION

In two previous papers, we developed a model of thermal Comptonization and disk thermal reprocessing to explain the data from recent multiwavelength monitoring observations of the type 1 Seyfert galaxies NGC 3516 and NGC 7469 (Chiang & Blaes 2001, hereafter Paper I; Chiang 2002, hereafter Paper II). The essential features of this model were proposed by Poutanen, Krolik, & Ryde (1997) to account for the different spectral states of the Galactic X-ray binary Cygnus X-1; and a simplified version was used by Zdziarski, Lubiński, & Smith (1999) to model the correlation seen in X-ray binaries and type 1 Seyfert galaxies between the X-ray spectral index and the relative strength of the Compton reflection continuum. A key element of this model is the feedback occurring between a centrally located Comptonizing plasma and the thin accretion disk that encircles it. The disk reprocesses X-rays from the central region, thus providing a significant fraction of the seed photons for the Comptonization process itself. For a given set of optical, UV, and X-ray data, this feedback mechanism determines the equilibrium state of the Comptonizing plasma. By computing the equilibria required by the NGC 3516 and NGC 7469 data, we found that the seemingly uncorrelated optical/UV and X-ray continuum variations exhibited by these sources could be described almost entirely in the context of this model. Furthermore, in modeling these variations, we were able to constrain the central black hole masses and the accretion rates of these objects; and we were able to compute the X-ray continuum at energies extending beyond  $\sim 20$  keV, a part of the spectrum that will soon be made more accessible by the *International Gamma-Ray Astrophysics Laboratory* (INTEGRAL).

During an intensive three day monitoring campaign in 1998 April with the *Rossi X-ray Timing Explorer* (RXTE), the *Advanced Satellite for Cosmology and Astrophysics* (ASCA), and the *Hubble Space Telescope*, NGC 3516 exhibited an optical continuum that was surprisingly constant, consisting of only  $\sim 3\%$  variations, while simultaneously showing  $\sim 60\%$  changes

in the 2–10 keV X-ray flux (Edelson et al. 2000). This apparent lack of response by the optical continuum to the changes in the X-ray flux has been taken as evidence against the thermal reprocessing model for the optical and UV variability. However, despite the relatively small amplitude of its fluctuations, the optical continuum varied essentially simultaneously across a wide range of wavelengths, in a manner consistent with disk thermal reprocessing (e.g., Krolik et al. 1991; Courvoisier & Clavel 1991; Collin-Souffrin 1991). In Paper I, we showed that a constant optical continuum in the presence of large X-ray fluctuations could be reconciled with the disk thermal reprocessing model if the radial extent,  $r_s$ , of the central Comptonizing plasma varied inversely with the X-ray luminosity,  $L_x$ , so that the flux incident upon the disk at moderately large radii remained constant. Slight departures from the  $L_x \propto r_s^{-1}$  relationship would then produce the highly correlated, low amplitude variations seen in the optical continuum of NGC 3516. We found that the range of X-ray fluxes and spectral indexes exhibited by this source is naturally accommodated by this behavior.

The interpretation of the NGC 7469 data is more complex. Data from a 30 day monitoring campaign in 1996 June–July with the *International Ultraviolet Explorer* (IUE) and RXTE showed that the UV continuum at  $\lambda 1350\text{\AA}$  and the 2–10 keV X-ray light curves were not correlated in any simple way (Nandra et al. 1998). Although the amplitude and time scales of the most prominent variations in the two datasets were comparable, some features in the UV occurred nearly simultaneously with similar looking features in the X-rays, while other features that were similar in the two light curves were offset by  $\sim 4$  days. A quantitative analysis revealed that the strongest correlation between the two light curves corresponded to the UV variations *leading* those of the X-rays by several days, contrary to naive expectations of the thermal reprocessing model. Nandra et al. (2000) were able to explain these data, at least qualitatively, by noting that the UV fluxes were highly correlated at near zero temporal lag with the X-ray spectral index and also

<sup>1</sup> University of Maryland, Baltimore County, JCA/Physics Dept. 1000 Hilltop Circle, Baltimore MD 21250

<sup>2</sup> Mailing Address: Stanford Linear Accelerator Center, MS 43A, 2575 Sand Hill Rd, Menlo Park CA 94025

with a broad band (0.1–100 keV) extrapolation of the 2–10 keV X-ray power-law. When we applied the thermal Comptonization/disk reprocessing model to these data, we found that rather large changes in the bolometric X-ray luminosity were required in order to produce the relatively large variations seen in the UV (Paper II). Since the X-ray continua for this source are relatively soft and are constrained in the 2–10 keV band by the *RXTE*/PCA observations, a broad range of temperatures for the Comptonizing electrons is needed so that the thermal Comptonization process can produce a concomitantly large range of X-ray luminosities.

Despite the difficulties associated with explaining these observations, the application of the model to these data yielded some encouraging results. First, the relatively large inner truncation radius of the thin disk,  $r_{\min} \sim 3 \times 10^{14}$  cm, that we found by fitting the optical and UV continuum data for NGC 7469 is consistent with that inferred from *ASCA* observations of the narrow iron  $K\alpha$  emission line by Guainazzi et al. (1994) if the broad line region reverberation mapping estimates of the black hole mass are correct (Peterson & Wandel 2000). Second, the value we inferred for the product of the black hole mass and accretion rate,  $\dot{M}M \sim 10^6 M_{\odot} \text{ yr}^{-1}$ , agrees with that found by Collier et al. (1998) who examined time delays between UV and optical continuum bands under the assumption of thermal reprocessing. Third, a global energy balance condition is satisfied by our models for both NGC 3516 and NGC 7469 wherein the total bolometric luminosity is consistent with the inferred accretion rate assuming nominal black hole masses of  $\sim 10^7 M_{\odot}$  for each source.

In the present paper, we analyze simultaneous optical, UV, and X-ray data for the Seyfert 1 galaxy NGC 5548 which were taken during two separate monitoring observations: a ground-based-optical/*IUE*/*Ginga* campaign in 1989–90 (Peterson et al. 1991; Clavel et al. 1991, 1992; Nandra et al. 1991) and our own 1998 ground-based-optical/*Extreme Ultraviolet Explorer* (*EUVE*)/*ASCA*/*RXTE* monitoring campaign (Chiang et al. 2000; Dietrich et al. 2001). Using our model, these data allow us to place limits on the mass and accretion rate of this object; and from that information, we can make predictions for what should be seen by *XMM-Newton* observations of this source in the optical, UV, and X-rays and by possible forthcoming simultaneous observations by *INTEGRAL* with other X-ray satellites such as *XMM-Newton*, the *Chandra X-ray Observatory*, and *RXTE*. In §2 of this paper, we describe the optical, UV, and X-ray data. In §3, we present our semi-analytic model of the spectral energy distributions (SEDs); and in §4, we derive constraints on the black hole mass and accretion rate. In §5, we show results from detailed Monte Carlo simulations of the thermal Comptonization and disk thermal reprocessing physics that verify the empirical relations we used in §3 and the SEDs we computed in §4. In §6, we discuss our results and their implications. We conclude in §7.

## 2. OBSERVATIONS OF NGC 5548

The simultaneous ground-based/*IUE*/*Ginga* observations of NGC 5548 cover a period Jan 1989 through July 1990. The *IUE* observations themselves took place from 1988 Dec to 1990 July and are described in Clavel et al. (1991) and Clavel et al. (1992). These references provide the continuum fluxes at the source rest frame wavelengths  $\lambda 1350\text{\AA}$ ,  $\lambda 1840\text{\AA}$ , and  $\lambda 2670\text{\AA}$ .

For the fluxes at the latter two wavelengths, we make the corrections for FeII and Balmer continuum contamination as described by Clavel et al. (1992; see also Wamsteker et al. 1990). The optical fluxes at  $\lambda 5100\text{\AA}$  were obtained via ground-based observations by Peterson et al. (1991). We correct for extinction for all these wave bands and for starlight contamination in the optical band as described in Magdziarz et al. (1998).

The *Ginga* data are from the monitoring campaign reported by Nandra et al. (1991) and were re-extracted by Magdziarz et al. (1998) to obtain additional effective area at the higher energies ( $\gtrsim 15$  keV). The re-extracted data cover energies from 1.7 to 30 keV. We have fit the *Ginga* data from the nine epochs that were simultaneous with the *IUE* observations using a power-law + reflection model for the continuum components (the PEXRAV model [Magdziarz & Zdziarski 1995] in XSPEC), a Gaussian function for the fluorescent iron  $K\alpha$  emission line, and a Galactic absorbing column fixed at  $N_H = 1.65 \times 10^{20}$  cm. In addition, we included an ionized absorber that is illuminated by a continuum with the same spectral index as the cut-off power-law (the ABSORI model [Done et al. 1992] in XSPEC). This latter component is required to model the absorption at energies below  $\sim 3$  keV that cannot be accounted for by the Galactic absorbing column alone. This spectral model is similar to that used by Magdziarz et al. (1998) to fit these same data. The difference is that we do not model the so-called “soft excess” since we do not find significant residuals below  $\sim 2.5$  keV that would indicate the need for a separate spectral component at these energies.<sup>3</sup> Nonetheless, we find very similar X-ray spectral indices and fluxes in the 2–10 keV band as do Magdziarz et al. (1998). The parameters from the fits to the *Ginga* data along with the corrected optical and UV fluxes are given in Table A1.

The simultaneous *EUVE*, *ASCA*, and *RXTE* observations took place in June–August 1998 and are described in detail in Chiang et al. (2000). For uniformity’s sake, we have used only spectral parameters obtained from fitting *RXTE*/PCA data. The *RXTE* observations covered a greater period of time than did the *ASCA* observations and overlapped more with the optical observations we discuss below. The PCA response matrices used in the original spectral analyses of these data were generated by the FTOOL utilities PCARMF V3.5 and PCARSP V2.36 (Chiang et al. 2000). However, the most recent versions of these programs as of September 2002, PCARMF V8.0 and PCARSP V8.0, produce response matrices that are sufficiently different from the earlier ones so that the newly fitted spectral indices differ from those presented in Chiang et al. (2000) by amounts that are  $\sim 3$ –4 times larger than the 90% confidence level statistical errors. In order to illustrate the effect of the systematic uncertainties implied by these changes, we have performed our analyses using the spectral parameters obtained for both sets of response matrices. In Table A3, the 2–10 keV fluxes and spectral indices are given for the “1999 PCA responses” and the “2002 PCA responses”. The former are taken directly from Table 6 of Chiang et al. 2000, while the latter have been determined for this paper.

In Table A3, the Compton reflection fractions,  $R$ , for each epoch are also presented. For the *RXTE* data, there is clearly a slight correlation between the reflection fraction and the photon spectral index such that the harder power-law spectra for the new fits are accompanied by weaker contributions from Comp-

<sup>3</sup> Magdziarz et al. (1998) were partly guided by non-simultaneous *ROSAT* data, which we do not use here. Only one epoch (7) of the *Ginga* data shows significant residuals above a power law at the softest X-ray energies.

ton reflection. However, the changes in  $R$  are not sufficiently large to account for the changes in the underlying spectral index.

Simultaneous UV fluxes do not exist for the 1998 *EUVE/ASCA/RXTE* observations, but we do have optical data at  $\lambda 5100\text{\AA}$  for seven of the epochs which were kindly provided to us by M. Dietrich (Dietrich et al. 2001). These data were extinction and starlight corrected as described in Magdziarz et al. (1998). The corrected flux values are given in Table A3. Unfortunately, the optical flux measurements were not all strictly simultaneous with the *RXTE* observations. For epoch 1.0, the flux listed in Table A3 was taken at JD-2450000 = 980.751, more than 8 hours after the *RXTE* observation window. For epochs 2.1–2.4, the optical measurements were taken either at the very beginning or the very end of the *RXTE* integration intervals which lasted from  $\sim 4$  to  $\sim 17$  hours. Given the uncertainties in the optical fluxes and the occasional sparseness of the coverage (see Dietrich et al. 2001, their Fig. 4), interpretation of these data as being simultaneous with the X-ray observations should be regarded with caution.

### 3. SEMI-ANALYTIC CALCULATIONS

As in Papers I and II, we consider a fairly simple model for the central regions of NGC 5548. A razor thin, flat accretion disk produces thermal emission that comprises the observed optical and UV continuum; and a centrally located, spherical Comptonizing region consisting of a plasma of hot electrons produces the power-law-like X-ray continuum detected at energies  $\sim 0.1$ – $100$  keV. The disk is truncated at an inner radius  $r_{\min} > 10 GM/c^2$ , the Comptonizing electrons are assumed to have a uniform temperature  $T_e$ , and the plasma sphere has a radius  $r_s \sim r_{\min}$ . Thermal emission from the disk enters the sphere and provides seed photons for the Comptonization process. In turn, X-rays from the sphere illuminate the disk, heating it, and thus causing it to produce thermal emission in excess of that resulting from local viscous dissipation. The feedback between the disk and sphere regulates the equilibrium temperature of the Comptonizing electrons, and variations in the geometry through changes in  $r_{\min}$  and/or  $r_s$  determine the spectral properties of the X-ray, optical, and UV continua. This sort of geometry for thermal Comptonization in active galactic nuclei (AGNs) and Galactic X-ray binaries has been explored in detail by a number of authors (e.g., Shapiro, Lightman, & Eardley 1976; Poutanen, Krolik, & Ryde 1997; Dove et al. 1997; Zdziarski, Lubiński, & Smith 1999).

We model the thermal emission from the surface of the accretion disk as

$$F_{\text{disk}} = F_{\text{visc}} + (1-a)F_{\text{inc}}, \quad (1)$$

where  $a$  is the disk albedo. The local flux produced by viscous dissipation is

$$F_{\text{visc}} = \frac{3}{8\pi} \frac{G\dot{M}\dot{M}}{r^3} \left[ 1 - \left( \frac{r_l}{r} \right)^{1/2} \right], \quad (2)$$

where  $r_l$  is the radius of the innermost stable circular orbit. Note that use of this expression assumes that the torque at the thin disk truncation radius  $r_{\min}$  is the same as that for a standard, untruncated thin disk with zero torque at  $r_l$ . We are also assuming that the disk is stationary, except for the variable heating resulting from the incident X-rays. This incident X-ray flux upon the disk is given as a function of radius by

$$F_{\text{inc}} = \frac{3}{16\pi^2} \frac{L_x}{r_s^2} h\left(\frac{r}{r_s}\right), \quad (3)$$

where  $L_x$  is the X-ray luminosity of the Comptonizing plasma, and the auxiliary function  $h(r/r_s)$  is given by Zdziarski et al. (1999; see also Paper II). This expression assumes that the X-ray emission is uniform, isotropic, and optically thin throughout the plasma sphere. The disk emission as seen by an observer at a luminosity distance  $d_l$  and an inclination  $i$  is given by

$$F_\nu = \frac{4\pi \cos i}{d_l^2} \frac{h\nu^3}{c^2} \int_{r_{\min}}^{\infty} \frac{r dr}{f_{\text{col}}^4 [\exp(h\nu/k_B T_{\text{disk}} f_{\text{col}}) - 1]}, \quad (4)$$

where the disk effective temperature is  $T_{\text{disk}} = (F_{\text{disk}}/\sigma_B)^{1/4}$ , and  $f_{\text{col}} = f_{\text{col}}(T_{\text{disk}})$  is a temperature dependent color correction appropriate for AGN disks (Paper II; see also Hubeny et al. 2001). In calculating  $d_l$ , we assume a Hubble parameter of  $H_0 = 67 \text{ km s}^{-1} \text{ Mpc}^{-1}$ .

The function  $h(r/r_s)$  can be approximated by

$$h\left(\frac{r}{r_s}\right) \simeq \frac{\pi}{4} \left(\frac{r}{r_s}\right)^{-3} \quad (5)$$

for  $r \gtrsim r_s$  (Zdziarski et al. 1999; see also Paper I), and therefore the disk thermal emission follows an  $\sim r^{-3}$  distribution whether it results from viscous dissipation or from reprocessing of the X-rays from the central plasma sphere, provided that  $r_s \sim r_{\min} \gtrsim 10 r_l$ . Under these circumstances, the disk surface temperature can be modeled as  $\tilde{T}_{\text{disk}} \simeq T_0(r/r_{\min})^{-3/4}$ . Using this approximation, we have obtained estimates of the disk inner truncation radius  $r_{\min}$  and the temperature  $T_0$  at this radius by fitting the optical and UV data with equation (4). Applying this procedure to the nine epochs of the 1989–90 data, we have found the  $r_{\min}$ -values listed in Table A2. These results depend sensitively on the disk inclination, and that dependence affects the inferred values for the other parameters describing the X-ray portion of the SEDs. We will explore the implications of this dependence in §5.

The underlying relationship between the X-ray luminosity, the black hole mass, and the accretion rate can be seen by using the approximation for  $h(r/r_s)$  (eq. [5]) and the aforementioned fits for  $r_{\min}$  and  $T_0$ . Since broad line region reverberation mapping estimates of the central black hole mass in NGC 5548 give  $M_{\text{rm}} = 6 \times 10^7 M_\odot$  (Peterson & Wandel 2000), and  $r_{\min} > 20 GM_{\text{rm}}/c^2$  for all nine of the 1989–90 epochs, we can neglect the term containing  $r_l/r$  in the expression for  $F_{\text{visc}}$  (eq. [2]). Using these approximations, the black hole mass and the accretion rate are related to the X-ray luminosity  $L_x$  and the radius of the plasma sphere  $r_s$  by

$$G\dot{M}\dot{M} + (1-a) \frac{L_x r_s}{8} = \frac{8\pi\sigma_B T_0^4 r_{\min}^3}{3}. \quad (6)$$

Since we are assuming that the disk is stationary (eq. [2]), the non-varying part of the optical/UV SED is modeled by the  $MM$  term on the left-hand side of equation (6), while any optical/UV variability in the model must be caused by changes in the thermal reprocessing component represented by the  $L_x r_s$  term and/or by changes in the truncation radius  $r_{\min}$ .

The values of  $L_x$  and  $r_s$  are also constrained by the observed 2–10 keV X-ray flux and spectral index, and by two energy balance conditions. The first energy balance condition follows from an empirical relation between the X-ray spectral index and the Compton amplification factor  $A$ , which is the ratio of the X-ray luminosity and the luminosity of “seed” photons,  $L_s$ , entering the Comptonizing plasma:

$$\Gamma = \Gamma_0 (A - 1)^{-1/\delta} \quad (7)$$

$$= \Gamma_0 \left( \frac{L_x}{L_s} - 1 \right)^{-1/\delta}. \quad (8)$$

The parameters  $\Gamma_0 = 2.15$  and  $\delta = 14$  have been found from fits to Monte Carlo calculations of the thermal Comptonization process (Malzac, Beloborodov, & Poutanen 2001; see also §4). If the seed photons consist only of thermal emission from the disk, then  $L_s$  is determined by the disk flux distribution  $F_{\text{disk}}(r)$  and by the geometry of the disk and Comptonizing plasma through  $r_s$  and  $r_{\text{min}}$ :

$$L_s = 4\pi \int_{r_{\text{min}}}^{\infty} g(\tilde{r}; \tilde{r}_s) I(r) r dr, \quad (9)$$

where  $I(r) = F_{\text{disk}}(r)/\pi$  is the disk surface brightness,  $\tilde{r} \equiv r/r_{\text{min}}$ , and  $g(\tilde{r}; \tilde{r}_s)$  is defined in Paper II and equals the fraction of isotropic emission that enters the central plasma sphere from a disk annulus  $(\tilde{r}, \tilde{r} + d\tilde{r})$ . Modeling the X-ray spectrum as an exponentially cut-off power-law,  $L_E \propto E^{1-\Gamma} \exp(-E/E_c)$ , where  $E_c \equiv 2k_B T_e$ , a value for  $L_x$  can be found using the 2–10 keV X-ray continuum flux,  $F_{210}$ , and X-ray spectral index,  $\Gamma$ :

$$L_x = \xi 4\pi d_l^2 F_{210} \frac{Q(\Gamma, E_{\text{min}}/E_c)}{Q(\Gamma, 2\text{keV}/E_c) - Q(\Gamma, 10\text{keV}/E_c)}. \quad (10)$$

Here  $E_{\text{min}} = 0.01$  keV is an assumed nominal lower cut-off energy, the precise value of which is not important for photon indices  $\Gamma < 2$ , and

$$Q(\Gamma, x) \equiv \int_x^{\infty} t^{1-\Gamma} e^{-t} dt. \quad (11)$$

Note that this expression is the incomplete gamma function. The factor  $\xi$  in equation (10) parameterizes any anisotropy in the thermal Compton emission. If this emission were isotropic and the plasma sphere were optically thin, then  $\xi = 1$ . Because photons from the first scattering order are preferentially scattered back towards the disk, the X-ray intensity incident upon the disk can be larger than the intensity seen by a distant observer (Paper II). Our Monte Carlo calculations show that  $\xi \simeq 1.5$  does a reasonable job of modeling this anisotropy for observer inclinations  $i \sim 30\text{--}45^\circ$  (see §4).

The second energy balance condition is more global in nature and comes from the expectation that the hot plasma is less efficient at radiating accretion power than a standard optically thick accretion disk would be in its place:

$$L_{\text{untr}} \gtrsim L_x + L_{\text{tr}}. \quad (12)$$

The quantities  $L_{\text{tr}}$  and  $L_{\text{untr}}$  are the luminosities resulting from viscous dissipation for a disk truncated at an inner radius  $r_{\text{min}}$  and an “untruncated” disk extending to the innermost stable circular orbit  $r_I$ , so that

$$L_{\text{tr,untr}} \equiv 4\pi \int_{r_{\text{min}}, r_I}^{\infty} r dr F_{\text{visc}}(r). \quad (13)$$

For a given value of  $r_I$ , equation (12) is equivalent to

$$L_x < \eta \dot{M} c^2 - L_{\text{tr}}, \quad (14)$$

where the efficiency  $\eta = 0.5$  for  $r_I = GM/c^2$ .<sup>4</sup> We generally assume that a firm upper limit to the X-ray luminosity is given by  $\eta = 1$ . Of course, this high a value would correspond to accretion efficiencies that exceed both that of the standard thin disk and those expected for other models such as advection dominated accretion flows (ADAFs; Narayan & Yi 1995). However, even higher efficiencies are conceivable if the spin energy of the central black hole can be tapped (e.g., Krolik 1999; Gammie 1999; Wilms et al. 2001).

To summarize, we effectively have five relations constraining the properties of the inner accretion flow. We list them here in terms of their functional dependence on the model parameters and the observationally determined quantities:

$$M\dot{M} = M\dot{M}(L_x, r_s, r_{\text{min}}; F_{\text{OUV}}), \quad (15a)$$

$$\Gamma = \Gamma(L_x, L_s; \Gamma_0, \delta), \quad (15b)$$

$$L_s = L_s(L_x, r_s, r_{\text{min}}, M\dot{M}), \quad (15c)$$

$$L_x = L_x(T_e; F_{210}, \Gamma), \quad (15d)$$

$$L_x < L_{\text{untr}}(M\dot{M}, r_I) - L_{\text{tr}}(M\dot{M}, r_{\text{min}}). \quad (15e)$$

The first relation represents equations (1–4) (or approximately eq. [6] by itself); and the remaining four relations represent equations (8), (9), (10), and (14), respectively. In these five relations, there are six unknowns<sup>5</sup>,  $L_x$ ,  $L_s$ ,  $T_e$ ,  $r_s$ ,  $M\dot{M}$ , and  $r_I$ ; and we consider the remaining quantities as being either directly measured from or constrained by the observations:  $F_{210}$  and  $\Gamma$  from the X-ray data, and  $r_{\text{min}}$  by the optical and UV data as represented by  $F_{\text{OUV}}$  (see eq. [4]). In order to obtain a unique solution to equations (15), additional information is necessary. Direct measurement of the roll-over energy  $E_c$  would provide the most useful constraints since that would provide estimates of both  $L_x$  and  $T_e$ , but instruments with the required sensitivity in the relevant energy range are not yet available. Reverberation mapping measurements of the black hole mass can be used to estimate  $r_I$ ; but as we will see below, the standard value for NGC 5548,  $M_{\text{rm}} = 6 \times 10^7 M_\odot$  (Peterson & Wandel 2000), yields accretion rates so low that equation (14) is violated or that imply electron temperatures that are inconsistent with the observed X-ray continua.

#### 4. RESULTS

In order to get a sense for how the quantities  $r_I$  and  $M\dot{M}$  can affect the implied solutions, we have solved equations (15a–d) numerically over a grid of values spanning  $M = (1\text{--}7) \times 10^7 M_\odot$  and  $M\dot{M} = (0.5\text{--}7.5) \times 10^5 M_\odot^2 \text{ yr}^{-1}$ , assuming  $r_I = GM/c^2$ . As an example, in Figure A1, the values of  $k_B T_e$  obtained from these fits are plotted versus  $M\dot{M}$  for the 1989–90 epoch 2 data. Since  $r_{\text{min}} = 1.8 \times 10^{14} \text{ cm} > 10 r_g$  over the entire range of masses, the  $r_I/r$  term in equation (1) plays a minor role in determining the disk flux distribution, and equation (6) roughly applies. Consequently, the electron temperatures are nearly independent of  $M$  and are determined mostly by the quantity  $M\dot{M}$ . This functional dependence is shown in Figure A1 by the various symbols (corresponding to the different masses) and by the single solid curve that connects the values of  $k_B T_e$  averaged over the masses at each  $M\dot{M}$  value. For each black hole mass, we compute the minimum accretion rate that satisfies equation (14),

$$\dot{M}_{\text{min}} \equiv \frac{L_x + L_{\text{tr}}}{\eta c^2}, \quad (16)$$

where we have taken the accretion efficiency to be  $\eta = 0.5$ . The dashed curves show the fitted  $k_B T_e$  values plotted versus  $M\dot{M}_{\text{min}}$  for the specified mass; solutions of equation 15a–d that also obey equation 15e will lie to the right of the dashed curves. Hence, the intersection of each dashed curve with the solid curve gives the minimum value of  $M\dot{M}$  that satisfies the energy balance condition (eq. [14]). That intersection point also

<sup>4</sup> This is obtained from equation (13). We do not use the more familiar value of  $\eta = 0.42$  since we are neglecting general relativistic effects throughout this work.

<sup>5</sup> In fact, the disk inclination  $i$  is another unknown. For clarity, we defer explicit discussion of it until §5 and assume  $\cos i = 0.7$  for our analyses of the NGC 5548 data unless otherwise indicated.

corresponds to the maximum electron temperature that can be achieved for the given mass. For  $M = 10^7 M_\odot$ , the electron temperature during epoch 2 must satisfy  $k_B T_e \lesssim 200$  keV; while for  $M = 6 \times 10^7 M_\odot$ , it must satisfy  $k_B T_e \lesssim 60$  keV.

Several observations of the same source in different flux states can place additional limits on the black hole mass  $M$  and accretion rate  $\dot{M}$ , provided the latter is fixed as we are assuming by adopting a stationary thin disk structure. As we described above, we use the optical and UV continuum fluxes to determine the disk inner radius,  $r_{\min}$ , in each epoch. In contrast to our previous studies of NGC 3516 and NGC 7469 (Paper II), the optical and UV data for NGC 5548 do seem to require variations in  $r_{\min}$ . This is evidenced by the relatively large optical/UV color changes occurring over these observations (Table A1). These observations are separated in time by intervals ranging from two days to nearly one year. If variations in  $r_{\min}$  result from viscous processes, then any feasible observational time scale would be far too short to expect significant changes. However, if the  $r_{\min}$ -variations occur because of thermal instabilities causing the disk to alternately “puff up” and then “deflate” near the innermost radius of the thin disk, then such variations could occur on a thermal time scale:

$$t_{\text{th}} \sim 10^6 \text{ s} \left( \frac{\alpha}{0.1} \right)^{-1} \left( \frac{r_{\min}}{2 \times 10^{14} \text{ cm}} \right)^{3/2} \left( \frac{M}{10^7 M_\odot} \right)^{-1/2}, \quad (17)$$

where  $\alpha$  is the anomalous viscosity parameter. This is roughly consistent with the time scales of the  $r_{\min}$ -variations listed in Table A2, except perhaps for the 2-day interval between epochs 4 and 5 that would require somewhat larger values of  $\alpha$  and/or black hole mass than are indicated in equation (17).

In Figure A2, we plot the  $k_B T_e$ - $MM$  curves for all nine of the 1989–90 epochs. The vertical dotted lines indicate the minimum  $MM$  values for epoch 1 assuming masses  $M = (1, 2, 3, 4, 5, 6, 7) \times 10^7 M_\odot$ , ordered left-to-right. These lower limits are greater than the corresponding ones found for the other eight epochs, and so they represent the most restrictive minimum values for  $MM$ . Given these lower limits, a black hole mass of  $M = 6 \times 10^7 M_\odot$  implies a minimum value of  $(MM)_{\min} \simeq 7.5 \times 10^5 M_\odot^2 \text{ yr}^{-1}$  and requires rather low electron temperatures for the eight other epochs, with  $k_B T_e \lesssim 20$  keV in all cases. For temperatures that low, the thermal roll-over would be detected in the X-ray spectra taken by instruments such as *Ginga* and *RXTE/PCA*, which have useful sensitivity up to  $\sim 20$ – $30$  keV for the brighter type 1 Seyfert galaxies. Of course, the degree to which these observations could detect the effects of a low electron temperature depends on the shape of the thermal Comptonization continuum. Although power-laws with exponential cut-offs are often used to model these spectra, detailed thermal Comptonization calculations, such as our Monte Carlo calculations (§ 5), generally show sharper high energy cut-offs so that the thermal roll-over may not be as evident at lower energies. Furthermore, a strong Compton reflection component can hide a low energy thermal roll-over much in the same way it can mask a softer underlying power-law index. Nonetheless, one can adopt a fairly conservative minimum value for  $T_e$  as an observational constraint. For our purposes, we will require  $k_B T_e > 30$  keV, which is indicated by the lower dotted horizontal line in Figure A2. Since the  $k_B T_e$ - $MM$  curves decline fairly rapidly, a much lower minimum temperature will not drastically alter the implied limits on  $M$  and  $\dot{M}$ . From Figure A2, we see that the epoch 7 and 9 curves constrain  $MM \lesssim 2.5 \times 10^5 M_\odot^2 \text{ yr}^{-1}$  and the black hole mass to be  $M < 2 \times 10^7 M_\odot$ . Since we expect the accretion efficiency

to be less than maximal, we will take  $M = 1 \times 10^7 M_\odot$  and  $\dot{M} = 2 \times 10^{-2} M_\odot \text{ yr}^{-1}$  as nominal values hereafter. Assuming  $r_I = GM/c^2$ , this yields  $L_{\text{untr}} = \dot{M} c^2 / 2 = 6 \times 10^{44} \text{ erg s}^{-1}$  as our heuristic upper-limit for the bolometric luminosity of this source (eq. [14]). Note that this is 60 percent of the Eddington luminosity at the chosen black hole mass, which would be difficult to reconcile with an ADAF interpretation for the inner accretion flow.

The model parameters and SEDs which we find for the 1989–90 data using these values are listed in Table A2 and shown in Figure A3, respectively. In all cases we find that  $r_s/r_{\min} \sim 1$ , with this ratio being slightly greater or slightly less than unity at different epochs. Note that values less than unity need not imply that there is a physical gap between the hot plasma and the inner truncation radius of the disk. Instead, it may indicate a central accretion flow that is more flattened and aspherical compared to the sphere we assume in the present model (see Paper II).

The SEDs shown in Figure A3 often have more power in the Comptonized X-ray component than in the optical/UV disk thermal component. This is still consistent with a radiatively inefficient hot inner flow, because that efficiency should be compared to a radiatively efficient disk at the same radius where most of the accretion power is generated. Indeed, the very fact that the X-rays appear to take up such a large fraction of the bolometric power is strongly suggestive of the accretion flow geometry we are considering here.

Applying our calculations to the 1998 observations is problematic since we lack the UV data required to constrain the disk inner radius. However, having ascertained  $M$  and  $\dot{M}$  from the 1989–90 data, we can explore the feasible range of disk inner radii for the 1998 epochs in light of our temperature constraint. In Figure A4, we plot the equilibrium electron temperature versus  $r_{\min}$  for the seven epochs of the 1998 data for both sets of response matrices. For clarity, we have plotted the individual curves that are obtained from analyses using the 1999 PCA response matrices; while for the 2002 response matrices, we simply show a hashed region that is bound by the minimum and maximum  $k_B T_e$  values at each value of  $r_{\min}$ .

Using the 1999 response matrices, the curve for epoch 2.2 requires that  $r_{\min} \leq 2.4 \times 10^{14} \text{ cm} (= 160 GM/10^7 M_\odot/c^2)$  in order to satisfy  $k_B T_e > 30$  keV. If we assume that this upper limit for  $r_{\min}$  applies to all of the 1998 observations, then the electron temperature for epoch 3.2 would be  $k_B T_e \gtrsim 1500$  keV (see Table A4). Since we do not consider pair-production or the possibility of a non-thermal component of relativistic electrons, another constraint we are tacitly imposing in this model is that the electron temperatures should satisfy  $k_B T_e \lesssim m_e c^2$ . For temperatures much greater than this, the thermalization time scales exceed the cooling time scales, and a non-thermal electron component will arise (Coppi 1999). The presence of a significant non-thermal component would invalidate the energy balance implied by the thermostatic interaction between the disk reprocessed radiation and the Comptonization emission from the hot plasma. Therefore, in order to satisfy this implicit upper limit for the temperature, the curves shown in Figure A4 suggest that the disk inner radii for these data span a range at least as wide as  $r_{\min} \simeq (2.4\text{--}3.2) \times 10^{14} \text{ cm}$ . However, for the spectral parameters derived using the 2002 response matrices, the disk inner radius can take *any single value* in the range  $(3.1\text{--}4.7) \times 10^{14} \text{ cm}$  for *all seven epochs* and still be consistent with electron temperatures that lie within our nominal range of

30–511 keV. Since  $r_s \sim r_{\min}$  for all these calculations (see Tables A4 and A5), it is worth noting that, despite the changes in the *RXTE*/PCA response matrices, all of these radii are roughly consistent with our estimates of the size of the Comptonizing region that we derived from the temporal lags between the soft (0.16 keV) and hard (2–10 keV) X-ray light curves of the 1998 *EUVE/ASCA/RXTE* observations (Chiang et al. 2000).

In Figure A5, we plot model spectral energy distributions for the seven 1998 ground-based/*RXTE* epochs. Two of the sets of curves have been computed using the parameters from the 1999 response matrix spectral fits, assuming  $r_{\min} = 2.4 \times 10^{14}$  cm (solid curves) and  $r_{\min} = 3.2 \times 10^{14}$  cm (dashed). The SEDs corresponding to the 2002 response matrix fits are also shown (dot-dashed curves) and have been computed assuming  $r_{\min} = 3.2 \times 10^{14}$  cm. The disk luminosities resulting from viscous dissipation are  $L_{\text{tr}} = 1.0 \times 10^{43}$  and  $0.7 \times 10^{43}$  erg s $^{-1}$  for  $r_{\min} = 2.4 \times 10^{14}$  cm and  $3.2 \times 10^{14}$  cm, respectively. Global energy balance, equation (14), is obeyed in all cases. The SEDs shown in Figure A5 illustrate the dramatic effect that the change in the response matrices have on the inferred broad band X-ray continuum. It is worth emphasizing, however, that the 2–10 keV continuum fluxes obtained using the two different sets of response matrices are fairly consistent with one another (see Table A3). Consequently, the largest differences in the model SEDs occur at energies that lie well outside the range directly measured by *RXTE*/PCA.

## 5. MONTE CARLO CALCULATIONS

We have implemented a three dimensional Monte Carlo calculation of the thermal Comptonization/thermal reprocessing model we have described in the previous section. A more detailed description appears in the Appendix and in Chiang & Blaes (2002). In this section, we compare results from our Monte Carlo calculations with the empirical relations we have used in the previous section and with the spectral energy distributions obtained using those semi-analytic methods.

In Figure A6, we plot the X-ray continuum spectral index versus the amplification factor,  $A = L_x/L_s$ . The individual data points are from our Monte Carlo calculations, the solid curve is the parameterization of Malzac et al. (2001; see eq. [8]), and the dashed curve is a best fit to the Monte Carlo data with  $\Gamma_0 = 2.06$  and  $\delta = 15.6$ . The filled triangles represent the Monte Carlo calculations that produced the histogrammed SEDs shown in Figure A3; we discuss these simulations in greater detail below. The other symbols represent simulations that were computed for a black hole mass of  $M = 2 \times 10^7 M_\odot$ , a disk inner radius  $r_{\min} = 2 \times 10^{14}$  cm, an observer inclination of  $i = 30^\circ$ , five mass accretion rates  $\dot{M} = 0, 0.01, 0.02, 0.04$ , and  $0.08 M_\odot \text{ yr}^{-1}$ , and five sphere radii  $r_s = 0.5, 0.75, 1.0, 1.25$ , and  $1.5 \times 10^{14}$  cm for a total of 25 spectra.

In Figure A7, we plot the ratio  $L_{s,\text{repr}}/L_{x,\text{app}}$  versus  $r_s/r_{\min}$  for these same two sets of simulations. Here  $L_{s,\text{repr}}$  is the seed photon luminosity produced by thermal reprocessing (i.e., the total  $L_s$  minus the portion produced by viscous dissipation), and  $L_{x,\text{app}}$  is the *apparent* thermal Comptonization luminosity, i.e., the luminosity one would compute from equation (10) for  $\xi = 1$ . The solid curve is the relation one would find if the thermal Comptonization luminosity were indeed isotropic so that the flux incident upon the disk is given by equation (3). The dashed curve is the solid curve multiplied by  $\xi = 1.5$ , the value we adopted to model the anisotropy of the thermal Comptonization emission. This factor also takes into account differences

in the albedo of the disk. For the semi-analytic calculations, we assumed a constant albedo of  $a = 0.15$ , while the disk albedos found in the Monte Carlo calculations vary with the incident spectrum, ranging from  $a \simeq 0.2$  for  $\Gamma \simeq 1.9$  to  $a \simeq 0.4$  for  $\Gamma \simeq 1.5$ . As can be seen from Figure A7, for  $r_s/r_{\min} \gtrsim 1.1$ , a value of  $\xi = 1.5$  is appropriate, while for lower values, which correspond to weaker coupling between the hot plasma and cold disk and therefore produce harder spectra, a value of  $\xi \simeq 1$  should probably be used.

In Figure A3, the histograms are the Monte Carlo SEDs we computed using the values of  $M$ ,  $\dot{M}$ ,  $r_s$ , and  $r_{\min}$  found in §3 for the 1989–90 data. The equilibrium electron temperatures we obtain from our Monte Carlo calculations are systematically larger by  $\sim 20\%$  than those from our semi-analytic methods. Now, in the Monte Carlo simulations, we have set the radial Thomson depth,  $\tau_r$ , of the Comptonizing sphere to be equal to the Thomson depth,  $\tau$ , found from the observed spectral index, the electron temperature from the semi-analytic method, and the empirical relation (Beloborodov 1999),

$$\Gamma = \frac{9}{4}y^{-2/9}, \quad (18)$$

where the Compton  $y$ -parameter is

$$y \equiv \tau(1 + \tau)4\theta_e(1 + 4\theta_e), \quad (19)$$

and  $\theta_e \equiv k_B T_e / m_e c^2$ . Since the spectral index is set by the geometric factors,  $r_s$  and  $r_{\min}$ ,  $\Gamma$  is independent of the Thomson depth of the plasma. However, the amplitude of the thermal Comptonization continuum is determined by the amount of seed photons *scattered* in the Comptonizing region and so should be roughly proportional to  $1 - e^{-\tau_r}$ . Therefore, the mismatch between the continuum levels of the semi-analytic and Monte Carlo calculations, most clearly seen in the epoch 5 results, can be reduced by adjusting the radial Thomson depth of the plasma sphere. This will, of course, result in different electron temperatures as well.

For the epoch 1 data, the shape of the Monte Carlo SED is more difficult to reconcile with the exponentially cut-off power-law used in our semi-analytic method because for sufficiently high electron temperatures the individual scattering orders are partially resolved in the X-ray spectra. This illustrates another, observationally-based motivation for an upper limit on the electron temperature. If the mean separation in energy between the peaks of individual scattering orders exceeds their width, these orders will be partially resolved in the resulting thermal Comptonization continuum and will appear as a number of spectral breaks and/or local maxima and minima (e.g., Skibo & Dermer 1995). Empirically, we find from our Monte Carlo calculations that an upper limit of  $k_B T_e \lesssim m_e c^2$  is required to prevent these features from appearing.

## 6. DISCUSSION

The wide range of electron temperatures,  $k_B T_e \sim 40\text{--}700$  keV, that we found for the ground-based/*IUE/Ginga* data is driven by the relatively broad range of optical/UV fluxes (see Table A1). In Paper II, we obtained similar results for the NGC 7469 monitoring observations, which also had large optical/UV variations. In that work, we were able to narrow the range of temperature changes that was required by allowing the X-ray spectral indices to vary within their  $1\text{-}\sigma$  uncertainties. For the NGC 5548 ground-based/*IUE/Ginga* data, the most conspicuous out-lier is the fit to the epoch 1 data. Those data yield an electron temperature that is at least three times larger than the temperatures

found for the other eight epochs. The epoch 1 data also have an unusually hard X-ray spectral index,  $\Gamma = 1.56$ . This value lies at the very low end of the range of spectral indices that are typical for type 1 Seyfert galaxies (Zdziarski, Poutanen, & Johnson 2000). Furthermore, it is substantially smaller than the indices of the other *Ginga* epochs (with the notable exception of epoch 8). However, as we noted in Paper II, softer spectra have less X-ray flux at energies  $> 10$  keV than do harder spectra for a given value of  $k_B T_e$  and a fixed 2–10 keV flux. In order to reduce  $k_B T_e$  for epoch 1, we would either have to make the X-ray spectrum even harder, i.e., use  $\Gamma < 1.56$ , or take a larger value of the 2–10 keV flux. Setting  $F_{210} = 3.73 \times 10^{-11}$  erg cm $^{-2}$ s $^{-1}$  for epoch 1, which corresponds to a 10% increase in 2–10 keV flux over the fitted value (see Table A1), we obtain a uniform 20% reduction in the equilibrium electron temperature for all values of  $\dot{M}$  considered. The resulting changes in the inferred minimum accretion rates are even smaller: for  $M = 7 \times 10^7 M_\odot$ ,  $\dot{M}_{\min}$  is reduced by 13%, while for  $M = 2 \times 10^7 M_\odot$ , the reduction is less than 4%.

For the preceding analyses of the NGC 5548 data we have assumed an observer inclination of  $i = 45^\circ$  ( $\cos i = 0.7$ ). Our calculations are surprisingly sensitive to this value. Since the optical/UV spectral shape for a given epoch is determined largely by the temperature of the disk at the innermost radius,  $T_0$  is independent of  $\cos i$ . The disk flux is proportional to  $\sim \cos i r_{\min}^2 T_0^4$ , so that for a given set of optical/UV data, we have  $r_{\min} \propto (\cos i)^{-1/2}$ . If the disk emission is dominated by the thermally reprocessed component, then the geometry is determined by the X-ray spectral index (Zdziarski et al. 1999), and we have  $r_s \propto r_{\min} \propto (\cos i)^{-1/2}$ ,  $L_s \propto T_0^4 r_{\min}^2 \propto (\cos i)^{-1}$ , and  $L_x \propto (\cos i)^{-1}$ . Inserting these relations into equation (6), we obtain

$$G\dot{M} = \frac{8\pi\sigma_B T_0^4 r_{\min,0}^3}{3(\cos i)^{3/2}} - \frac{L_{x,0} r_{s,0}(1-a)}{8(\cos i)^{3/2}}, \quad (20)$$

where  $L_{x,0}$ ,  $r_{\min,0}$ , and  $r_{s,0}$  are fiducial values evaluated for  $\cos i = 1$ . The implied values of  $\dot{M}$  will therefore be larger for smaller  $\cos i$ . Similarly, the global energy balance condition (eq. [14]) allows us to obtain a  $(\cos i)$ -scaling for  $\dot{M}$ :

$$\eta \dot{M} c^2 > \frac{4\pi\sigma_B T_0^4 r_{\min,0}^2}{\cos i} + [1 - (1-a)R] \frac{L_{x,0}}{\cos i}, \quad (21)$$

where  $R$  is the fraction of the X-ray luminosity intercepted by the disk. Taking the minimum value for  $\dot{M}$  in order to have a maximum value for the black hole mass, this expression and equation (20) imply  $M \propto (\cos i)^{-1/2}$  and  $\dot{M} \propto (\cos i)^{-1}$ . Now, the X-ray observations and our ad hoc limits for the electron temperature fix the range of thermal Comptonization roll-over energies, and therefore they essentially fix the  $L_x$  values for the 1989–90 data as a whole (see Figs. A2 and A8), so the second term on the right-hand side of equation (20) will, in practice, go as  $(\cos i)^{-1/2}$ . Nevertheless, the general trend for  $M$  and  $\dot{M}$  to be larger for smaller values of  $\cos i$  still holds. In fact, we find for these data that each term on the right-hand side of equation (20) is much larger than the left-hand side, so given the different effective scalings with  $\cos i$  of those two terms, the value of  $\dot{M}$  is quite sensitive to the assumed inclination.

Figure A8 illustrates more concretely how much the feasible ranges of  $M$  and  $\dot{M}$  depend on the choice of the observer inclination; we show plots of  $k_B T_e$  versus  $\dot{M}$  for  $i = 30^\circ$  and  $i = 60^\circ$  for the 1989–90 data. If we take our minimum electron temperature limit seriously, then for  $i = 30^\circ$ , we find  $M \lesssim 2 \times 10^6 M_\odot$  and  $\dot{M} \lesssim 2 \times 10^4 M_\odot \text{yr}^{-1}$ . By contrast, for  $i = 60^\circ$ , we find

$M \lesssim 3 \times 10^7 M_\odot$  and  $\dot{M} \lesssim 6 \times 10^5 M_\odot \text{yr}^{-1}$ . In the latter case, an electron temperature of  $k_B T_e \simeq 1200$  keV is implied for epoch 1, which well exceeds our upper temperature limit. For the former case, although the electron temperatures fall within our adopted limits of  $30 \text{ keV} < k_B T_e < m_e c^2$ , the implied black hole mass is a factor of 30 smaller than the reverberation mapping estimate. Therefore, as a compromise, we have taken  $i \simeq 45^\circ$  as our nominal value which does yield a somewhat high electron temperature ( $k_B T_e \simeq 700$  keV) for epoch 1, but also gives a mass upper limit ( $M < 2 \times 10^7 M_\odot$ ) that is not in too great conflict with the reverberation mapping estimates (see Krolik 2001). Note that extraction of black hole spin energy, which we have not considered here, would ease the upper limits on the black hole mass by allowing, in principle, accretion efficiencies in excess of unity.

Even assuming a mass as large as the reverberation mapping estimates, our fits to the optical/UV continua give  $r_{\min} > 20 GM/c^2$ . This is marginally inconsistent with the range of disk inner radii of  $r_{\min} = 7.5\text{--}15 GM/c^2$  found by fitting a relativistically broadened iron line to the 1998 ASCA data (Chiang et al. 2000; see also Mushotzky et al. 1995). If  $M \lesssim 2 \times 10^7 M_\odot$ , then our results would be in serious disagreement with the detection of a relativistically broadened line. This conclusion relies on the 1989–90 epoch 1 data providing the relevant limits on  $\dot{M}$ . It is clear from Figures A2 and A3 that the SED during this epoch was unusual, and the source may have been in a transient state for which the X-ray luminosity briefly exceeded the limit imposed by equation (14). Averaging over the nine 1989–90 epochs, we obtain a much lower set of  $\dot{M}$ -limits than we find from epoch 1 alone. These are indicated in Figure A2 by the arrows along the top of the plot. We still require that  $\dot{M} \lesssim 2.5 \times 10^5 M_\odot \text{yr}^{-1}$  in order to have reasonable electron temperatures for epochs 7 and 9; and so these averaged limits imply  $M \lesssim 3 \times 10^7 M_\odot$ . If we take  $M = M_{\text{rm}} = 6 \times 10^7 M_\odot$ , then  $\dot{M} \lesssim 4.2 \times 10^{-3} M_\odot \text{yr}^{-1}$  and  $\dot{M} c^2/2 = 1.2 \times 10^{44}$  erg s $^{-1}$ . In this case, the X-ray luminosity exceeds the limit imposed by global energy balance for all observations except epoch 9.

If the Comptonizing plasma is an ADAF, then the radial velocity of the accretion flow in this region is  $v_r \sim \alpha v_\phi$ , substantially higher than that of the surrounding thin disk (Narayan & Yi 1995). From mass conservation and our estimates of the accretion rate, we can determine a characteristic Thomson depth,  $\tau_c$ , for the central region. Mass conservation in an accretion disk is given by

$$\dot{M} = 2\pi r v_r \Sigma \quad (22)$$

$$\sim 4\pi r^2 \rho v_r, \quad (23)$$

where  $\Sigma = 2h\rho$  is the disk surface density,  $h$  is the half-thickness, and we have set  $h \sim r$  for the central region which we assume to be dominated by ions at the virial temperature. The density of the central region is roughly

$$\rho \sim \frac{\tau_c}{r_s \kappa_e}, \quad (24)$$

where  $\kappa_e = 0.4 \text{ cm}^2 \text{g}^{-1}$  is the electron scattering opacity. Solving equations (23) and (24) for the Thomson depth and inserting nominal values, we obtain

$$\tau_c \sim 0.4 \left( \frac{\alpha}{0.1} \right)^{-1} \left( \frac{r_s}{2 \times 10^{14} \text{ cm}} \right)^{-1/2} \times \left( \frac{M}{2 \times 10^7 M_\odot} \right)^{-3/2} \left( \frac{\dot{M}}{2.5 \times 10^5 M_\odot \text{yr}^{-1}} \right). \quad (25)$$

Despite the crudeness of this estimate, it is encouraging that  $\tau_c$  lies within the range of Thomson depths yielded by our model (Tables A2, A4, and A5).

A potentially serious problem for this model is the large change in Thomson depth that we find between epochs 2.1 and 2.2 of the 1998 observations for both sets of response matrices (Tables A4 and A5). Since changes in  $r_{\min}$  must occur on time scales that are at least as long as the thermal time scale and since epochs 2.1–2.4 are fairly closely spaced over a 240 ks period (Chiang et al. 2000; see also Table A3), we must adopt a single radius for these epochs. For the 1999 response matrices and assuming  $r_{\min} = 2.4 \times 10^{14}$  cm, the Thomson depth must change from  $\tau = 0.06$  to  $\tau = 2.26$  over  $\sim 30$  ks. Even for the 2002 response matrices, the Thomson depth must change from  $\tau = 0.21$  to 0.69, assuming  $r_{\min} = 3.2 \times 10^{14}$  cm. The necessity for these large changes can be readily understood. During these epochs, the  $\lambda 5100\text{\AA}$  flux was essentially constant (Table A3). As we found for NGC 3516, in order to have a nearly constant optical flux, the radius of the Comptonizing region has to maintain an inverse relationship with the X-ray luminosity (eq. [6]). Since the X-ray spectral index increased over this interval, the radius  $r_s$  also had to increase in order to produce a softer spectrum; and therefore  $L_x$  had to decrease. However, the 2–10 keV X-ray flux increased at the same time, and so the electron temperature had to decrease by a very large amount to compensate. For a fixed Thomson depth, the electron temperature after the transition would result in an X-ray spectrum that would be much softer than is observed, and so the Thomson depth had to change substantially as well. The time scale for the evolution of the Thomson depth of the central region should be limited by either the thermal or accretion (i.e., viscous) time scales. Assuming a virial temperature for the ions in the central region, these two time scales are approximately the same,  $t_{\text{acc}} \sim t_{\text{th}} \sim 10^6$  s (eq. [17]).

One possible mitigating factor here is the relatively sparse coverage of the optical observations (see §2). Multiplying the optical fluxes for epochs 2.1–2.4 in Table A3 by the factors 0.86, 1.14, 1.07, and 0.98, respectively, yields a nearly constant Thomson depth of  $\tau = 0.44$  and electron temperatures  $k_B T_e \simeq 169\text{--}184$  keV, assuming  $r_{\min} = 2.4 \times 10^{14}$  cm. Unfortunately, a  $> 28\%$  change in the  $\lambda 5100\text{\AA}$  flux over the  $\sim 30$  ks separating epochs 2.1 and 2.2 does not seem to be supported by the data (Dietrich et al. 2001, see their Fig. 4). Of course, it is the UV photons produced near the innermost radius of the thin disk that are most important for determining the energy balance of the Comptonizing plasma, and they may not be well correlated with the emission at longer wavelengths on these time scales. The disk flux at  $\lambda 5100\text{\AA}$  is produced at a characteristic radius of  $r_{5100} \sim r_{\min} [T_0 / (0.29 \text{ cm K} / 5.1 \times 10^{-5} \text{ cm})]^{4/3} \sim 3 \times 10^{15}$  cm. Therefore, the optical emission should be smeared out and delayed relative to the UV emission by  $\sim 10^5$  s.

## 7. CONCLUSIONS

We have fit simultaneous optical, UV, and X-ray data of NGC 5548 with reasonable success over a wide range of continuum flux levels using just a crude model consisting of a stationary, truncated accretion disk and a spherical hot inner plasma. Under fairly general assumptions concerning accretion efficiency, energy balance, and self-consistency, we are able to place upper limits on the black hole mass,  $M \lesssim 2 \times 10^7 M_\odot$  and the accretion rate,  $\dot{M} \lesssim 2.5 \times 10^5 M_\odot \text{ yr}^{-1} / M$ . The upper limit on the black hole mass is less than that derived from reverbera-

tion mapping, which may itself be subject to some systematic uncertainty. Increasing the accretion efficiency, perhaps by extracting black hole spin energy, would relax our constraint on the black hole mass. We also find that the disk truncation radius is of order the size of the Comptonizing plasma and is  $\sim 2\text{--}5 \times 10^{14}$  cm. This is remarkably consistent with the size scale inferred in a completely different manner from the measured EUV to X-ray time lags (Chiang et al. 2000).

Although the present model does not provide a perfect description of the multiwavelength variability of NGC 5548, these calculations do show the potential for using multiwavelength data for constraining properties of the disk/black hole system in these objects. Wider spectral coverage with more sensitive X-ray observatories will help enormously in testing models such as this. In particular, the ability to measure the thermal Comptonization roll-over at energies  $\gtrsim 50$  keV will allow us to abandon our ad hoc temperature limits and the assumption of a global energy balance condition. Forthcoming *INTEGRAL* observations are the best near-term prospects for better measuring the thermal Comptonization roll-over in Seyfert 1 galaxies; and some of the stronger sources — NGC 4151, IC 4329A, and MCG–6-30-15 — are among its highest priority targets. However, even *INTEGRAL* does not have the sensitivity to measure changes in the roll-over energy on the required time scales of  $\sim 30$  ks. For this, an instrument such as the hard X-ray detector aboard *ASTRO-E2* is required.

*XMM-Newton* observations of NGC 5548 alone may be able to provide stringent tests of this model. If the iron  $K\alpha$  line is relativistically broadened, then the EPIC detectors aboard *XMM-Newton* should be able to determine both the disk inclination  $i$  and the disk inner radius,  $r_{\min}$ , in units of  $GM/c^2$ . Combined with optical/UV spectroscopy available from the *XMM-Newton* Optical Monitor that can determine  $r_{\min}$  directly, such observations should be able to constrain the black hole mass. However, if  $r_{\min} \gg GM/c^2$ , as suggested by our analysis of the NGC 5548 data, then the iron line will not be relativistically broadened, and *XMM-Newton* observations will provide at best a weak upper limit on  $M$ .

We wish to emphasize again that our model assumes that the disk itself is stationary, and all optical/UV variability is a result of the variable incident X-ray flux and varying  $r_{\min}$ . As we noted in equation (17), the disk can be out of thermal equilibrium in the innermost regions on time scales comparable to the observed variations. If thermal instabilities are responsible for the variations in  $r_{\min}$ , then our model may not be fully consistent. Even in the optically emitting regions, the thermal time scale is only  $\sim 2 \text{ yr } (\alpha/0.1)^{-1}$  for a black hole mass of  $10^7 M_\odot$ . It may therefore be interesting to develop our model further to incorporate a non-stationary disk structure.

We thank Matthias Dietrich and Mike Eracleous for providing optical data from ground-based observations of NGC 5548, and we are grateful to Pawel Magdziarz for making available the re-extracted *Ginga* data. We thank the referee, Andrzej Zdziarski, for helpful comments and criticisms of the manuscript and for pointing out the changes in the calculation of the *RXTE*/PCA response matrices. We thank Jim Dove for providing calculations from his thermal Comptonization Monte Carlo code; and we thank Jim and Mike Nowak for helpful conversations on the applicability of these calculations to AGN observations. We acknowledge early work with Andrew Frey to model the effect of a changing disk truncation radius on the op-



tical/UV variability of NGC 5548. J.C. was partially supported by NASA ATP grant NAG 5-7723. O.B. acknowledges support from NASA ATP grant NAG-7075. This research has made use of data obtained from the High Energy Astrophysics Science Archive Research Center (HEASARC), provided by NASA's

Goddard Space Flight Center; and it has also made use of the NASA/IPAC Extragalactic Database (NED) which is operated by the Jet Propulsion Laboratory, California Institute of Technology, under contract with NASA.

## APPENDIX

### DESCRIPTION OF THE THERMAL COMPTONIZATION MONTE CARLO

Seed photons from the disk are drawn assuming that the disk radial temperature profile is set by contributions from local viscous dissipation and reprocessing of X-ray flux from the hot plasma. The intensity of the emission is assumed to be isotropic at each point on the surface of the disk, and the energy distribution of the photons is modified from black body to account for the temperature dependent empirical color correction we have applied (see §3 and Paper II). For disk photons which intercept the central Comptonizing region, the optical depth is computed using the full Klein-Nishina cross-section and assuming a single-temperature relativistic Maxwellian distribution for the electrons (Poutanen & Svensson 1996). A scattering location along the photon path is drawn from the appropriate distribution; and if the photon is scattered, then its subsequent trajectory and energy are drawn from the scalar Compton redistribution function (Poutanen & Svensson 1996; Jones 1968). The optical depth to the boundary of the Comptonizing region is computed and a new scattering location is drawn. This continues until the photon escapes the Comptonizing region.

If the escaping photon intercepts the disk, then a separate Compton reflection Monte Carlo is employed. In this calculation, the incident photon strikes a semi-infinite slab of material at the appropriate angle and is scattered by the cold electrons in the slab until it either re-emerges or is absorbed. For the material composing the slab, we adopt the absorption cross-sections and abundances of Bałucińska-Church & McCammon (1992), and assume that the hydrogen and helium atoms are fully ionized and the remaining elements are neutral. This part of the code is functionally identical to the Monte Carlo calculations used by Magdziarz & Zdziarski (1995) to derive parameterizations of the Compton reflection Green functions. We have tested our code against their expressions and find consistent reflection spectra. Photons that escape the Comptonizing region without hitting the disk and those that emerge from the disk without re-entering the plasma are included in the final spectra according to their energy and direction.

The thermal Comptonization part of our Monte Carlo code has been checked against a two-dimensional iterative scattering (IS) code in which the integrals for the source functions at each scattering order are computed numerically. This IS code has in turn been checked against the one-dimensional IS code of Poutanen & Svensson (1996). We confirm that our Monte Carlo calculation agrees at each scattering order with the IS code. Using the Monte Carlo code rather than the IS code presents several advantages. The principal one is that it runs more quickly than the IS code, within a certain accuracy, allowing us to explore parameter space more efficiently. Furthermore, interfacing it with the Compton reflection part of the code is easier since both methods deal with individual photons. Lastly, should we decide to generalize this calculation, it would be a straight-forward matter to modify the geometry of the Comptonizing region or take into account curved spacetimes in computing the trajectories of the photons.

In order to find the equilibrium temperature of the Comptonizing electrons, we proceeded iteratively, using the difference between the model and observed fluxes at a nominal wavelength (in this case,  $\lambda 5100\text{\AA}$ ) as the main convergence criterion. For the calculation of an individual spectrum, the radial Thomson depth  $\tau_r$ , the radius of the Comptonizing region  $r_s$ , the disk inner radius  $r_{\min}$ , the central black hole mass, the accretion rate, and initial estimates of the electron temperature and X-ray luminosity are taken from our semi-analytic calculations of §3. For the first iteration, we assume a nominal value for the disk albedo, and we use the expressions from Zdziarski et al. (1999), modified to include the contribution from local viscous dissipation, to determine the effective temperature as a function of disk radius. On subsequent iterations, the model and observed optical fluxes are compared, and the electron temperature (and therefore the X-ray luminosity) is adjusted. Since we are computing the Compton reflection spectrum in the disk at each iteration, we obtain the disk albedo as a function of radius which we use as input for the subsequent iteration. Convergence has been achieved when both the model optical flux agrees with the observed value and the X-ray flux has converged to within a specified tolerance—typically 5% for each. As with our semi-analytic calculations, our Monte Carlo calculations do not consider pair balance or the presence of a non-thermal component in determining the properties of the Comptonizing plasma.

## REFERENCES

- Balućńska-Church, M., & McCammon, D. 1992, *ApJ*, 400, 699
- Beloborodov, A. M. 1999, in *High Energy Processes in Accreting Black Holes*, eds. J. Poutanen and R. Svensson, (San Francisco: Astronomical Society of the Pacific), 295
- Chiang, J., et al. 2000, *ApJ*, 528, 292
- Chiang, J., & Blaes, O. 2001, *ApJ*, 557, L15 (Paper I)
- Chiang, J., & Blaes, O. 2002, in *Proc. JHU/LHEA Workshop on X-ray Emission from Accretion onto Black Holes*, ed. T. Yaqoob and J. H. Krolik, published electronically at [http://www.pha.jhu.edu/groups/astro/workshop2001/papers/chiang\\_j.ps](http://www.pha.jhu.edu/groups/astro/workshop2001/papers/chiang_j.ps)
- Chiang, J. 2002, *ApJ*, 572, 79 (Paper II)
- Clavel, J., et al. 1991, *ApJ*, 366, 64
- Clavel, J., et al. 1992, *ApJ*, 393, 113
- Collier, S., et al. 1998, *ApJ*, 500, 162
- Collin-Souffrin, S. 1991, *A&A*, 249, 344
- Coppi, P. S. 1999, in *High Energy Processes in Accreting Black Holes*, eds. J. Poutanen and R. Svensson, (San Francisco: Astronomical Society of the Pacific), 375
- Courvoisier, T. J.-L., & Clavel, J. 1991, *A&A*, 248, 389
- Dietrich, M., et al. *A&A*, 371, 79
- Done, C., Mulchaey, J. S., Mushotzky, R. F., & Arnaud, K. A. 1992, *ApJ*, 395, 275
- Dove, J. B., Wilms, J., & Begelman, M. C., 1997, *ApJ*, 487, 747
- Edelson, R. E., et al. 2000, *ApJ*, 534, 180
- Gammie, C. F. 1999, *ApJ*, 522, L57
- Guainazzi, M., Matsuoka, M., Piro, L., Mihara, T., & Yamauchi, M., 1994, *ApJ*, 436, L35
- Hubeny, I., Blaes, O., Krolik, J. H., Agol, E. 2001, *ApJ*, 559, 680
- Jones, F. C. 1968, *Phys. Rev.*, 167, 1159
- Krolik, J. H., et al. 1991, *ApJ*, 371, 541
- Krolik, J. H. 1999, *ApJ*, 515, L73
- Krolik, J. H. 2001, *ApJ*, 551, 72
- Magdziarz, P., & Zdziarski, A. A. 1995, *MNRAS*, 273, 837
- Magdziarz, P., et al. 1998, *MNRAS*, 301, 179
- Malzac, J., Beloborodov, A. M., & Poutanen, J. 2001, *MNRAS*, 326, 417
- Mushotzky, R. F., et al. 1995, *MNRAS*, 272, L9
- Nandra, K., et al. 1991, *MNRAS*, 248, 760
- Nandra, K., et al. 1998, *ApJ*, 505, 594
- Nandra, K., et al. 2000, *ApJ*, 544, 734
- Narayan, R., & Yi, I. 1995, *ApJ*, 452, 710
- Peterson, B. M., et al. 1991, *ApJ*, 368, 119
- Peterson, B. M., & Wandel, A. 2000, *ApJ*, 540, L13
- Poutanen, J., & Svensson, R. 1996, *ApJ*, 470, 249
- Poutanen, J., Krolik, J. H., & Ryde, F. 1997, *MNRAS*, 292, L21
- Shapiro, S. L., Lightman, A. P., & Eardley, D. N. 1976, *ApJ*, 204, 187
- Skibo, J. G., Dermer, C. D. 1995, *ApJ*, 455, L25
- Wamsteker, W., et al. 1990, *ApJ*, 354, 446
- Wilms, J., et al. 2001, *MNRAS*, 328, L27
- Zdziarski, A. A., Lubiński, P., & Smith, D. A., 1999, *MNRAS*, 303, L11
- Zdziarski, A. A., Poutanen, J., & Johnson, W. N., 2000, *ApJ*, 542, 703

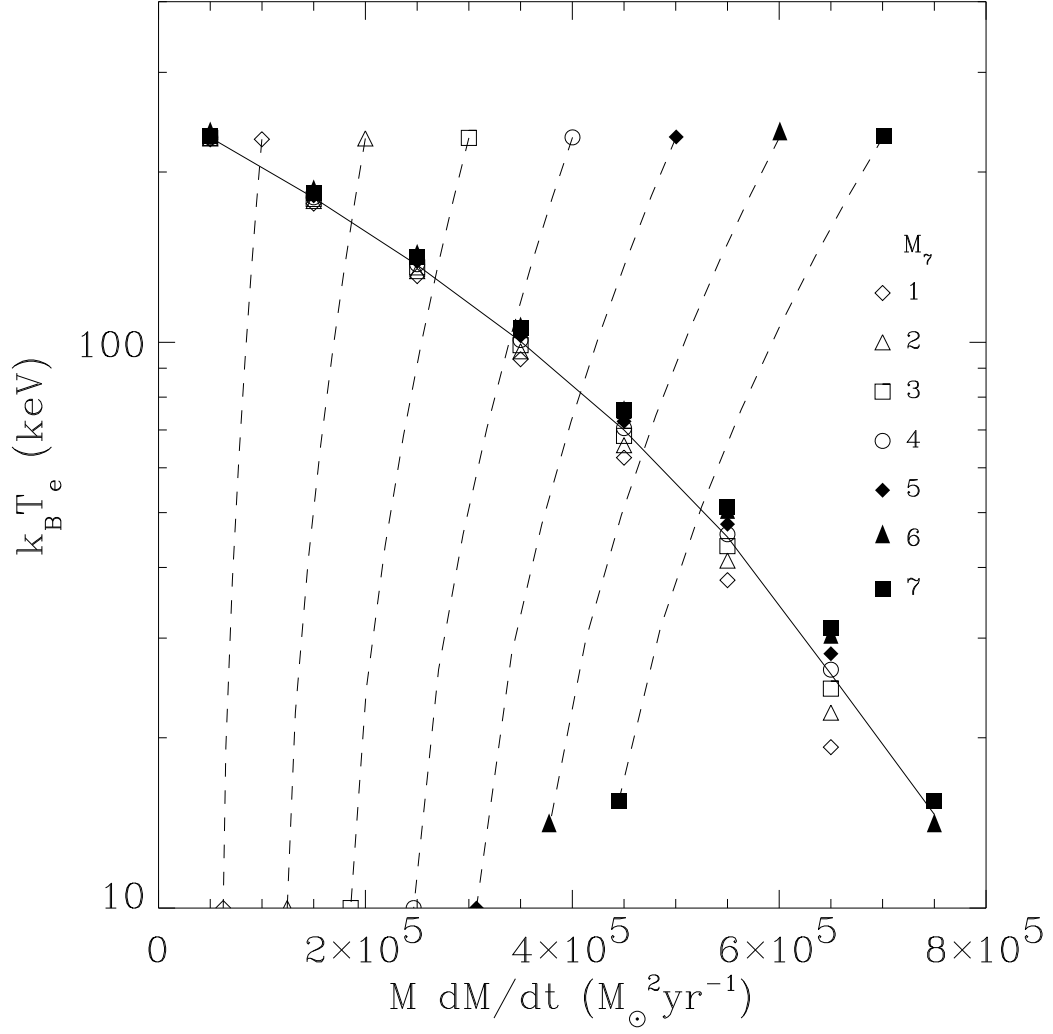


FIG. A1.— Equilibrium electron temperature,  $k_B T_e$ , versus  $M \dot{M}$  for the 1989–90 epoch 2 data, plotted as different clusters of points from the upper left to the bottom right. Each cluster corresponds to a different chosen value of  $M \dot{M} = (0.5, 1.5, 2.5, 3.5, 4.5, 5.5, 6.5, 7.5) \times 10^5 M_\odot^2 \text{yr}^{-1}$ . Within each cluster the different point symbols correspond to different black hole masses of  $M_7 \equiv M/(10^7 M_\odot) = (1, 2, 3, 4, 5, 6, 7)$ , as indicated in the figure. Note that  $k_B T_e$  depends primarily on  $M \dot{M}$ , with only a weak dependence on  $M$  arising because of the resulting variation in  $r_l$  (see eq. [2]). The solid curve shows the relation between  $k_B T_e$  and  $M \dot{M}$  after we have averaged over this weak mass dependence within each cluster of points. The dashed curves represent constraints from global energy balance, for different values of black hole mass as indicated by the point symbols at the ends of these curves. Each of these dashed curves shows  $k_B T_e$  vs  $M \dot{M}_{\min}$ , where  $\dot{M}_{\min} \equiv (L_x + L_{\text{tr}})/(\eta c^2)$  and  $\eta = 0.5$ . For a given black hole mass, the intersection of the dashed curve with the solid curve gives the minimum accretion rate and maximum electron temperature (see §4) that are consistent with equations 15a–e.

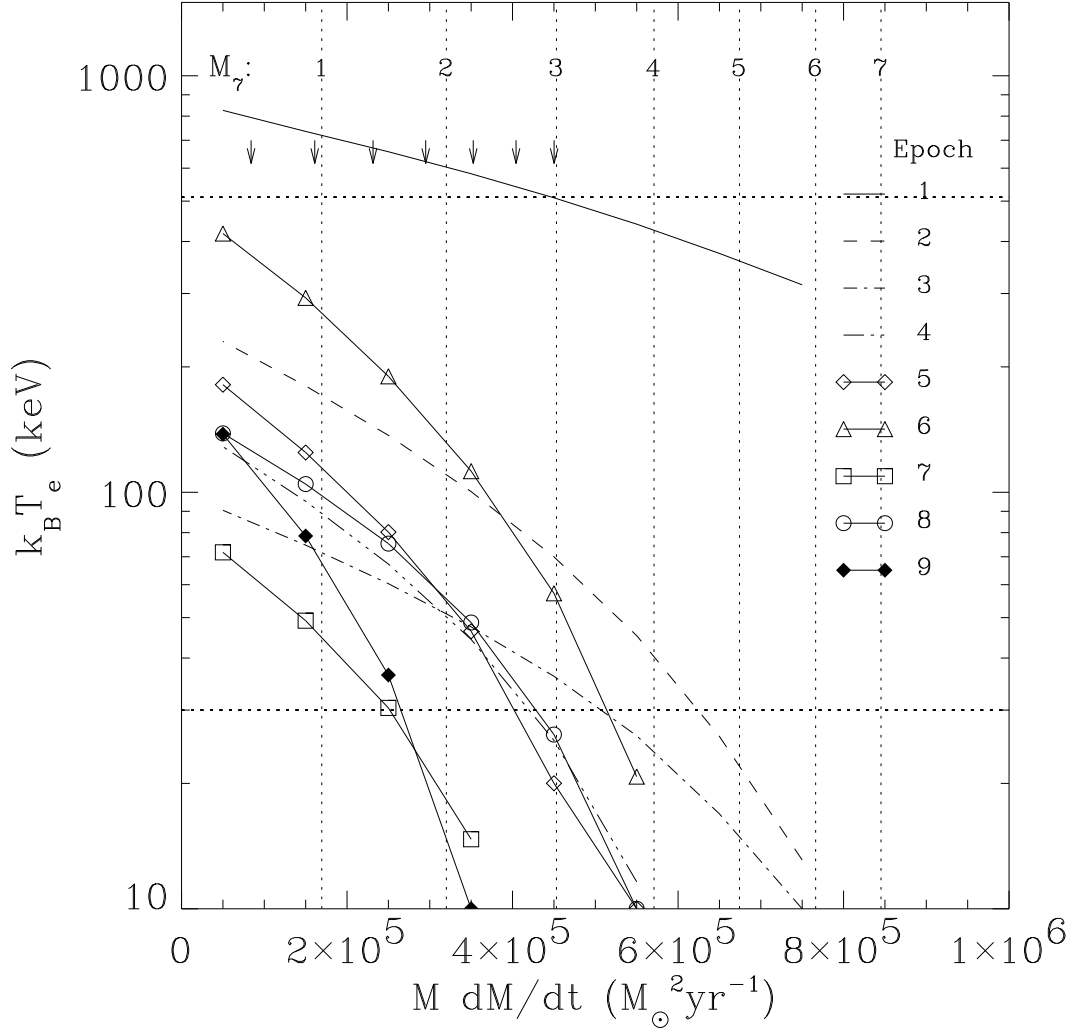


FIG. A2.— Electron temperature versus  $M\dot{M}$  for all nine 1989–90 epochs. The  $k_B T_e$  values for a given  $M\dot{M}$  have been averaged over the seven black hole masses considered in Figure A1. The  $k_B T_e$ - $M\dot{M}$  curves for each epoch are identified by the combination of line styles and symbols as shown in right-hand side of this figure. The dotted vertical lines indicate the minimum value of  $M\dot{M}$  for each mass for the epoch 1 data, which are the most constraining. These lines correspond to black hole masses  $M = (1, 2, 3, 4, 5, 6, 7) \times 10^7 M_\odot$ , ordered left-to-right and labeled near the top of the plot. The dotted horizontal lines show our assumed limits on the electron equilibrium temperatures,  $k_B T_{e\min} = 30$  keV and  $k_B T_{e\max} = m_e c^2 = 511$  keV. If we require  $k_B T_e \gtrsim 30$  keV for all nine epochs, then the  $k_B T_e$ - $M\dot{M}$  curves for epochs 7 and 9 constrain the black hole mass to be  $M < 2 \times 10^7 M_\odot$  and  $M\dot{M} \lesssim 2.5 \times 10^5 M_\odot^2 \text{yr}^{-1}$ . The arrows near the top of the plot indicate the minimum  $M\dot{M}$ -values averaged over the constraints for all nine epochs and correspond to  $M = (1, 2, 3, 4, 5, 6, 7) \times 10^7 M_\odot$ , ordered left-to-right. Therefore, taken as a whole, the optical/*IUE*/*Ginga* data require  $M \lesssim 3 \times 10^7 M_\odot$ .

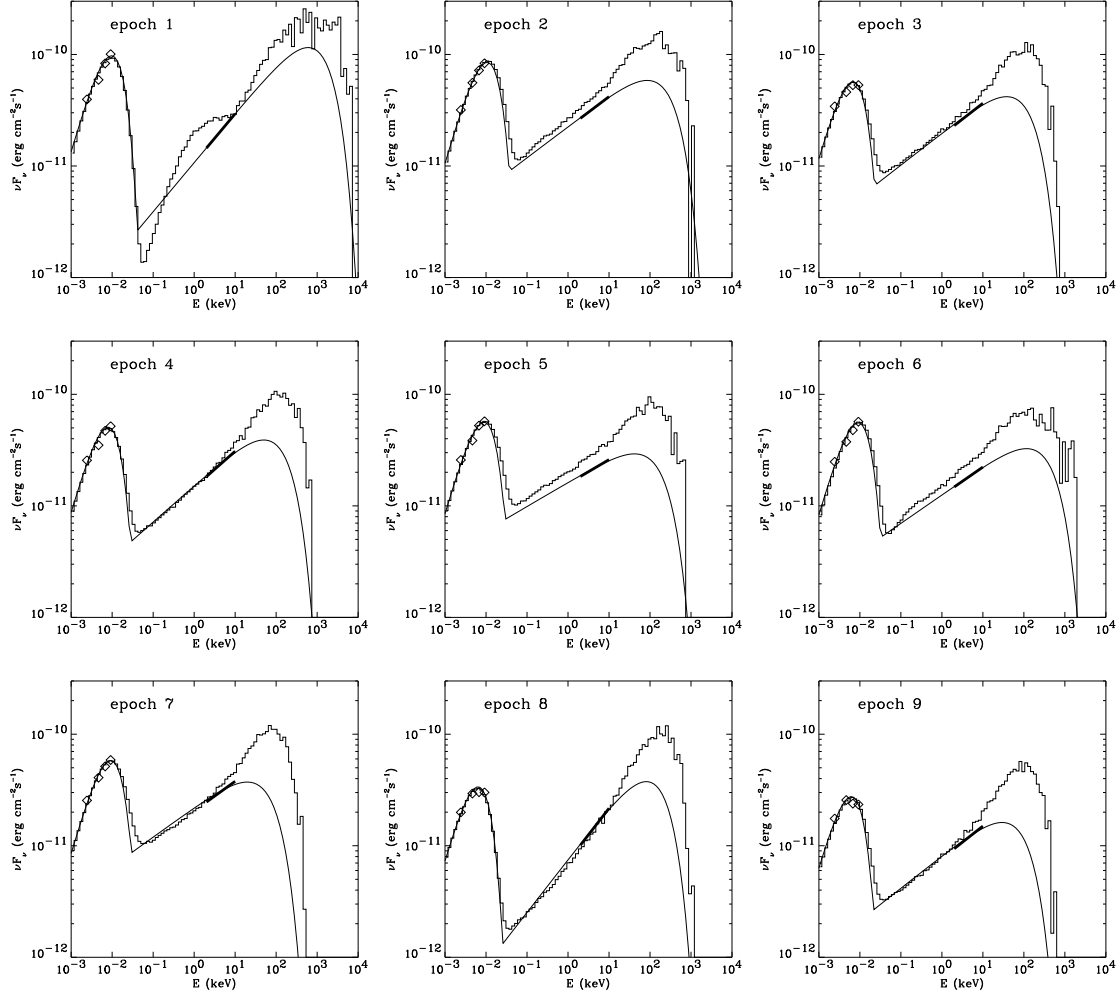


FIG. A3.— Spectral energy distributions which have been “fit” to the optical, UV, and X-ray data for the nine 1989–90 epochs. The optical/UV data are plotted as the open diamonds and the power-law fits to the 2–10 keV *Ginga* data are plotted as the thick line segments. The solid curves are the SEDs obtained from our semi-analytic calculations described in §3, and the histograms are the thermal Comptonization/thermal reprocessing Monte Carlo results using the parameters,  $r_s$ ,  $r_{\min}$ , and  $\tau_I = \tau$ , from the semi-analytic calculations (see §4). All these SEDs have been computed assuming  $M = 1 \times 10^7 M_\odot$  and  $\dot{M} = 0.02 M_\odot \text{ yr}^{-1}$ .

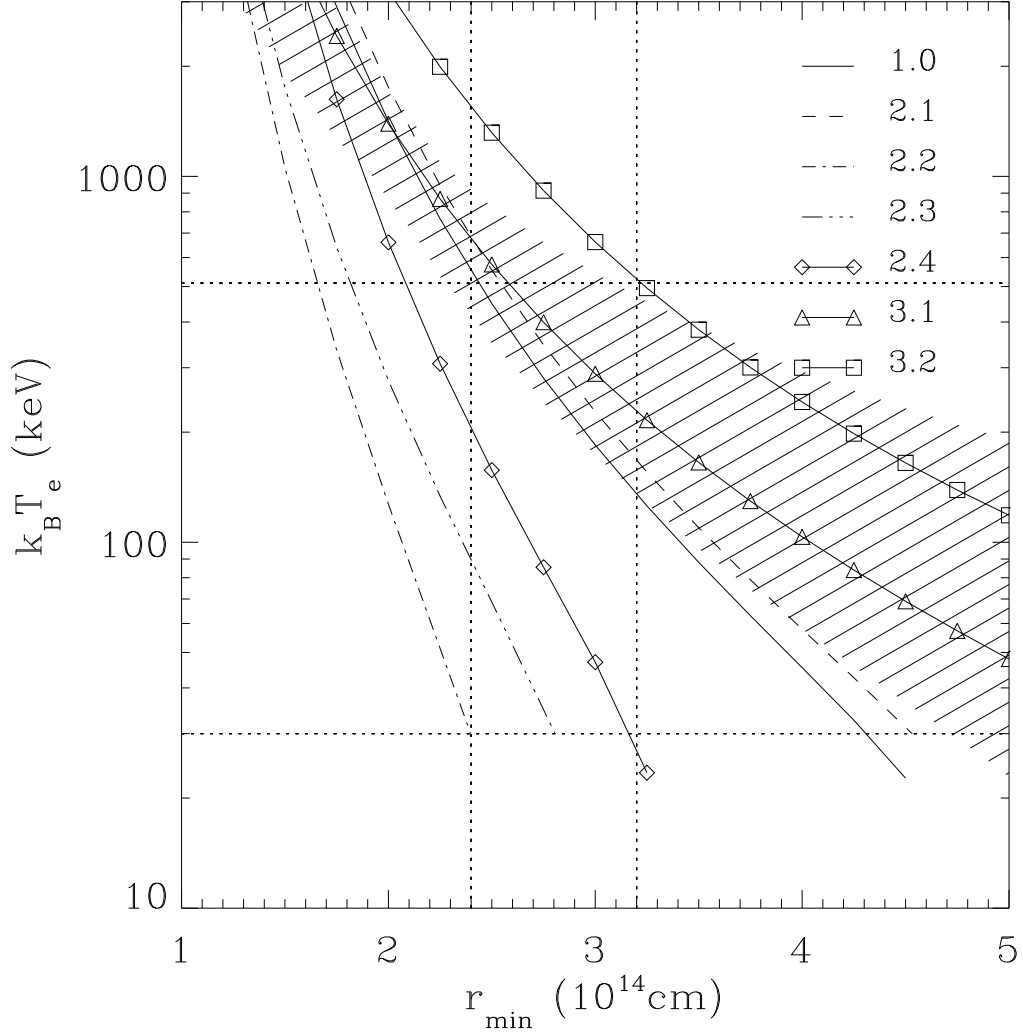


FIG. A4.—  $k_B T_e$  versus  $r_{\min}$  for the seven epochs of 1998 ground-based/RXTE data. The mass and accretion rate have been fixed at  $M = 1 \times 10^7 M_\odot$  and  $\dot{M} = 0.02 M_\odot \text{ yr}^{-1}$ . The horizontal dotted lines are our assumed upper and lower limits for the electron temperature,  $k_B T_{e\max} = 511 \text{ keV}$  and  $k_B T_{e\min} = 30 \text{ keV}$ . The individual curves have been obtained using the 1999 RXTE/PCA response matrices. The lower limit  $k_B T_{e\min}$  and the epoch 2.2 curve imply a maximum disk inner radius of  $r_{\min} \lesssim 2.4 \times 10^{14} \text{ cm}$  (leftmost vertical dotted line). By contrast, the upper limit  $k_B T_{e\max}$  and the epoch 3.2 curve require a *minimum* disk inner radius,  $r_{\min} \gtrsim 3.2 \times 10^{14} \text{ cm}$  (rightmost vertical dotted line). Taken together, these constraints imply that the disk inner radius had to vary significantly over the course of the 1998 observations. The hashed region shows the range of  $k_B T_e$  values at each  $r_{\min}$  that are obtained using the 2002 RXTE/PCA response matrices. For these fits, a single value of  $r_{\min}$  in the range  $(3.1\text{--}4.7) \times 10^{14} \text{ cm}$  may be taken for all seven epochs and will be consistent with our nominal upper and lower electron temperature limits.

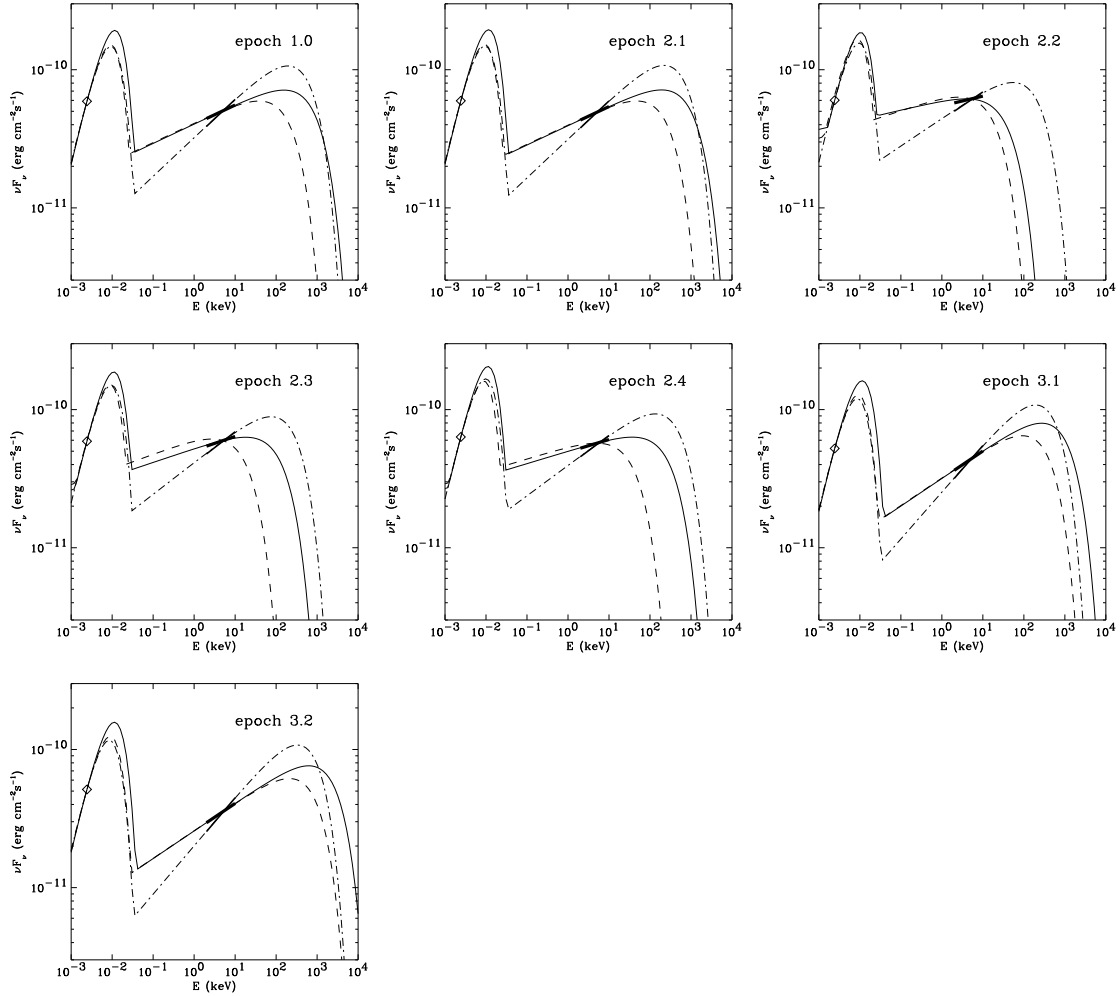


FIG. A5.— Model spectral energy distributions for the 1998 ground-based/RXTE data. Using the 1999 response matrices, SEDs have been computed for two inner disk radii,  $r_{\min} = 2.4 \times 10^{14}$  cm (solid curves) and  $r_{\min} = 3.2 \times 10^{14}$  cm (dashed curves). The differences in thermal Comptonization cut-off energy and the location and magnitude of the spectral peak in the UV band can be clearly seen. In epochs 2.2–2.4, the equilibrium electron temperatures are all  $< 30$  keV if one assumes a disk inner radius of  $r_{\min} = 3.2 \times 10^{14}$  cm. For an exponentially cut-off power-law with  $E_c = 2k_B T_e$ , these spectra differ substantially from the single power-law component inferred for the 2–10 keV band from the *RXTE*/PCA data (thick solid line segment). The SED calculations using the 2002 response matrices are shown as dot-dashed curves and a thinner line segment is plotted showing the 2–10 keV power-law for these data.

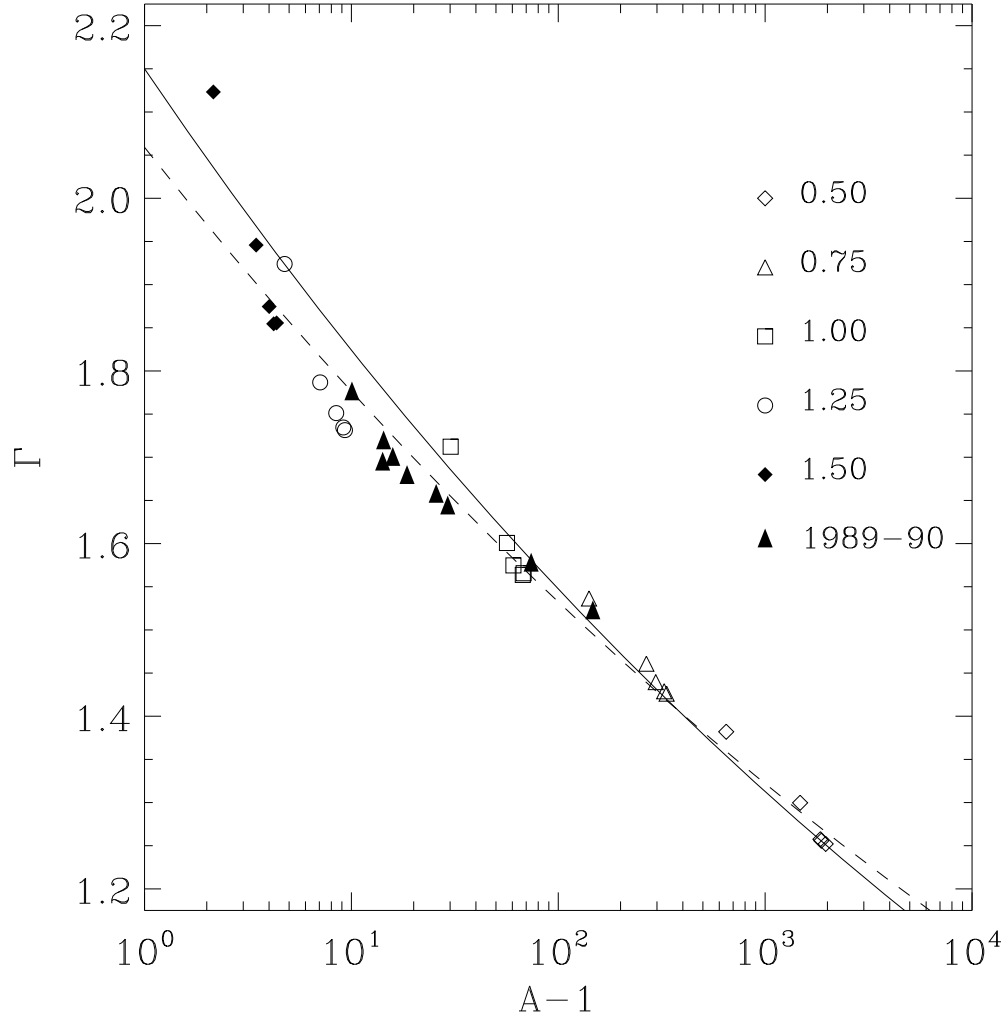


FIG. A6.—Photon spectral index versus Compton amplification factor minus unity. The filled triangles are from the Monte Carlo calculations shown in Figure A3 that were computed using the parameters for the 1989–90 data. The other symbols correspond to separate sets of Monte Carlo calculations for geometries with values of  $r_s/r_{\min} = 0.5, 0.75, 1, 1.25$ , and  $1.5$ , as indicated in the figure. Each set of Monte Carlo calculations had  $M = 2 \times 10^7 M_\odot$  and different values of  $\dot{M} = 0, 0.01, 0.02, 0.04$ , and  $0.08 M_\odot \text{ yr}^{-1}$ , with larger  $\dot{M}$  values corresponding to larger values of spectral index  $\Gamma$ . (For larger values of  $\dot{M}$ , smaller fractions of soft photons from thermal reprocessing are required, and so softer X-ray spectra are produced.) The solid curve is the parameterization found by Malzac et al. (2001) which has  $\Gamma_0 = 2.15$  and  $\delta = 14$  (see eq. [8]), while the dashed curve is the best fit to the Monte Carlo data yielding  $\Gamma_0 = 2.06$  and  $\delta = 15.6$ .



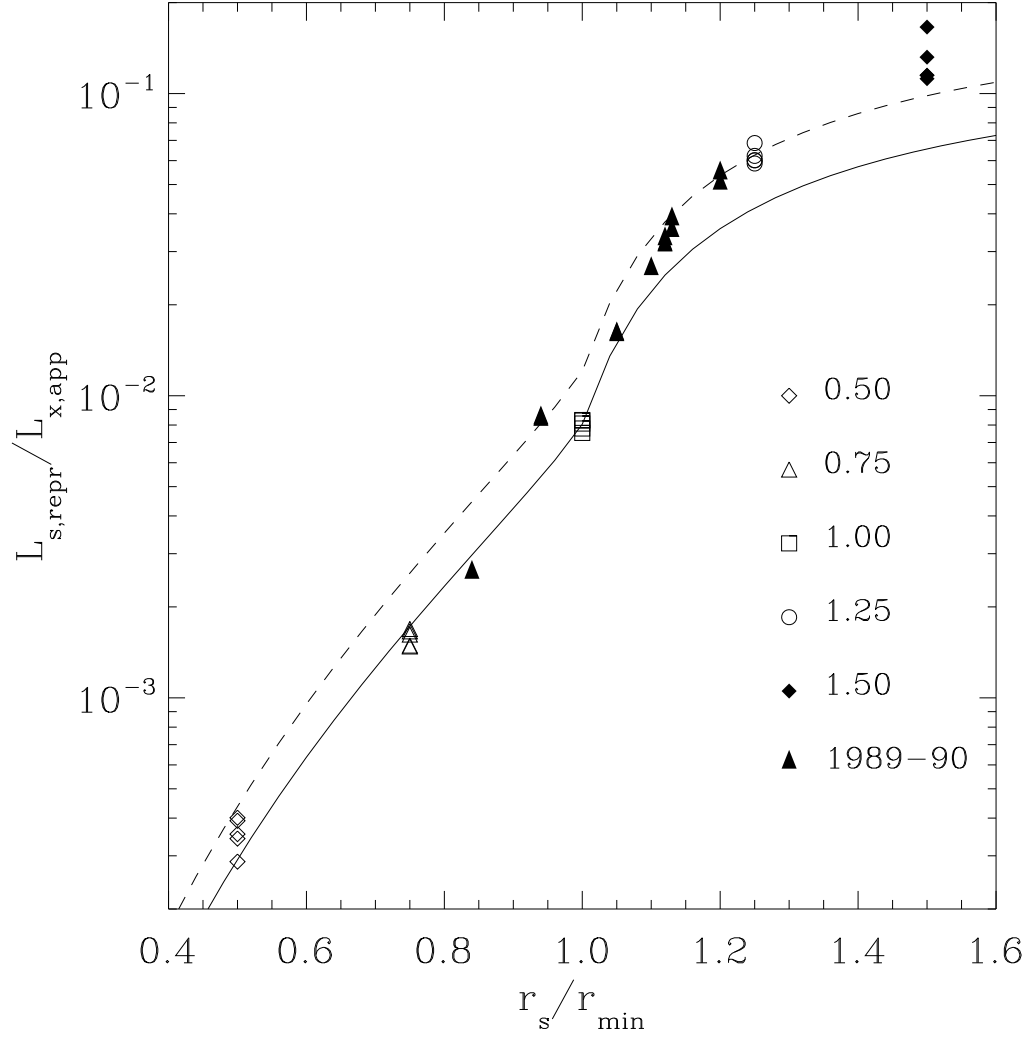


FIG. A7.— The ratio of the luminosity of thermally reprocessed seed photons,  $L_{s,\text{repr}}$ , to the apparent X-ray luminosity,  $L_{x,\text{app}}$ , versus the ratio of Comptonizing sphere radius,  $r_s$ , to disk inner radius,  $r_{\text{min}}$ . The data points are the Monte Carlo calculations, and the various symbols correspond to the same datasets,  $r_s/r_{\text{min}}$  and *Ginga* data, as in Figure A6. The solid curve is the relation obtained assuming the thermal Compton emission is isotropic. The dashed curve is the solid curve multiplied by  $\xi = 1.5$ .

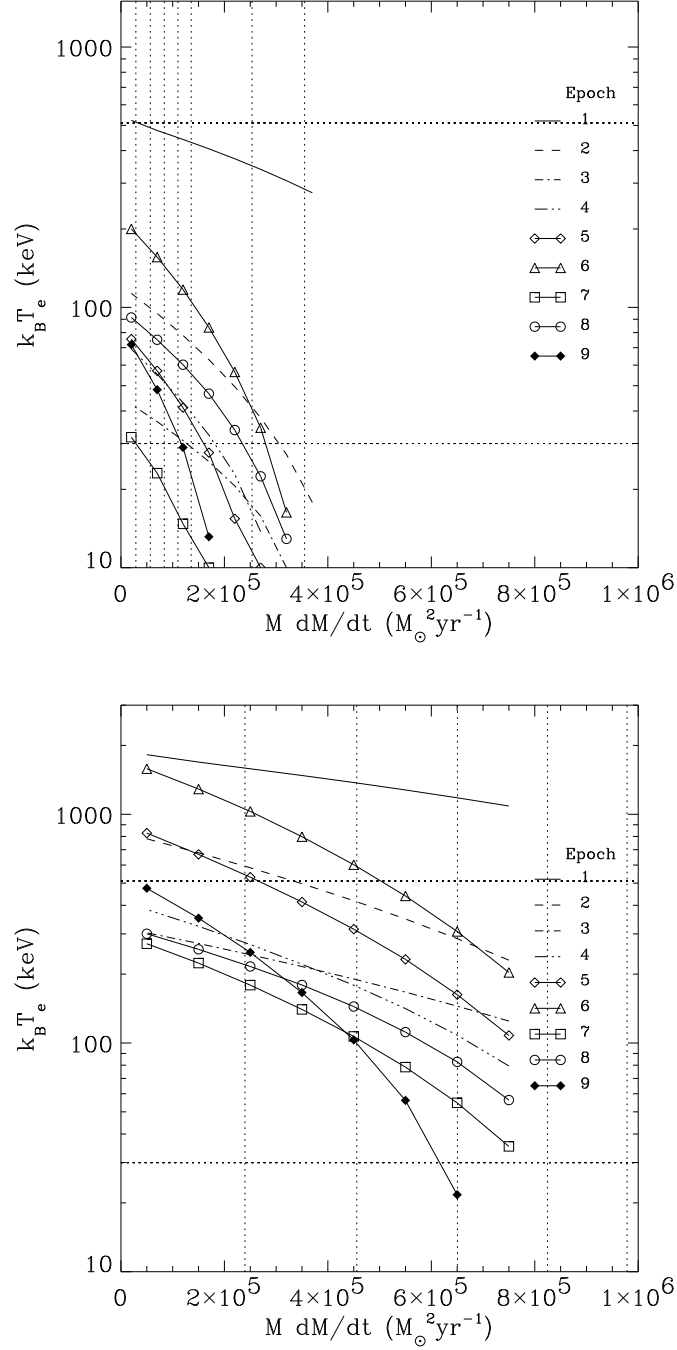


FIG. A8.— $k_B T_e$  versus  $M \dot{M}$  for two different observer inclinations,  $\cos i = 0.866$  (upper) and  $\cos i = 0.5$  (lower). These plots illustrate the sensitivity of the limits on the black hole mass and accretion rates to the assumed disk inclination. For  $\cos i = 0.866$ , the dotted vertical lines are the minimum  $M \dot{M}$ -values for black hole masses  $M = 0.2, 0.4, 0.6, 0.8, 1, 2, 3 \times 10^7 M_{\odot}$ , ordered left-to-right, while for  $\cos i = 0.5$ , the dotted vertical lines correspond to  $M \dot{M}$  limits for  $M = 1, 2, 3, 4, 5 \times 10^7 M_{\odot}$ . In both cases, these limiting values are from the epoch 1 curve. The horizontal dotted lines indicate  $k_B T_{e\min} = 30$  keV and  $k_B T_{e\max} = 511$  keV.

TABLE A1

OPTICAL AND UV CONTINUUM FLUXES AND X-RAY CONTINUUM PARAMETERS FROM THE 1989–90 GROUND-BASED/*IUE/Ginga* DATA.

epoch	JD–2440000	$F_{5100}^a$	$F_{2670}^a$	$F_{1840}^a$	$F_{1350}^a$	$F_{210}^b$	$\Gamma^c$	$R^{c,d}$
1	7535–7539	$0.78 \pm 0.08$	$2.22 \pm 0.19$	$4.52 \pm 0.22$	$7.45 \pm 0.33$	3.39	$1.56 \pm 0.19$	$0.32^{+0.72}_{-0.31}$
2	7556	$0.62 \pm 0.06$	$2.09 \pm 0.20$	$3.91 \pm 0.22$	$6.18 \pm 0.33$	5.43	$1.72 \pm 0.03$	$0.58 \pm 0.20$
3	7685	$0.67 \pm 0.06$	$1.72 \pm 0.23$	$2.88 \pm 0.31$	$3.94 \pm 0.46$	4.71	$1.71 \pm 0.10$	$0.44^{+0.41}_{-0.31}$
4	8036–8037	$0.50 \pm 0.06$	$1.31 \pm 0.36$	$2.56 \pm 0.30$	$3.84 \pm 0.35$	3.87	$1.68 \pm 0.06$	$0.28^{+0.24}_{-0.12}$
5	8039–8041	$0.51 \pm 0.07$	$1.44 \pm 0.25$	$2.85 \pm 0.36$	$4.25 \pm 0.42$	3.53	$1.78 \pm 0.06$	$0.97^{+0.52}_{-0.42}$
6	8047	$0.49 \pm 0.07$	$1.40 \pm 0.19$	$2.59 \pm 0.30$	$4.21 \pm 0.35$	2.94	$1.75 \pm 0.08$	$0.97^{+0.72}_{-0.39}$
7	8056	$0.50 \pm 0.06$	$1.53 \pm 0.17$	$2.80 \pm 0.21$	$4.35 \pm 0.24$	4.95	$1.74 \pm 0.04$	$0.38^{+0.24}_{-0.20}$
8	8068	$0.39 \pm 0.05$	$1.10 \pm 0.13$	$1.64 \pm 0.30$	$2.23 \pm 0.35$	2.44	$1.53 \pm 0.04$	$< 0.27$
9	8077	$0.34 \pm 0.05$	$0.96 \pm 0.20$	$1.30 \pm 0.30$	$1.74 \pm 0.35$	1.93	$1.71 \pm 0.14$	$0.87^{+0.99}_{-0.60}$

<sup>a</sup>Units are  $10^{-14}$  erg cm $^{-2}$ s $^{-1}$ Å $^{-1}$ . The flux uncertainties are 1- $\sigma$ .<sup>b</sup>Units are  $10^{-11}$  erg cm $^{-2}$ s $^{-1}$ . Throughout this paper, the 2–10 keV flux is computed for the *underlying* X-ray continuum which is assumed to be a cut-off power-law in the PEXRAV model. Therefore, these fluxes exclude the Fe K $\alpha$  emission, the Compton reflection component, and corrects for the effects of absorption.<sup>c</sup>Uncertainties are computed for  $\Delta\chi^2 = 2.706$ .<sup>d</sup>Compton reflection fraction.

TABLE A2

MODEL PARAMETERS FIT TO THE 1989–90 GROUND-BASED/*IUE/Ginga* DATA ASSUMING  $M = 1 \times 10^7 M_\odot$ ,  $\dot{M} = 0.02 M_\odot \text{ YR}^{-1}$ , AND  $\cos i = 0.7$ . NOTE THAT  $r_{\min}$  AND  $T_0$  DEPEND ONLY ON  $\cos i$ .

epoch	$r_{\min}^a$	$T_0$ ( $10^4$ K)	$r_s^a$	$k_B T_e$ (keV)	$\tau$	$L_x^b$	$L_{\text{tr}}^b$
1	2.20	4.0	2.07	683	0.13	4.65	0.11
2	1.85	4.2	2.07	153	0.72	3.03	0.13
3	3.36	2.8	3.70	66	1.64	2.10	0.07
4	2.31	3.3	2.42	76	1.54	1.84	0.10
5	2.07	3.6	2.47	96	1.05	1.68	0.11
6	1.97	3.7	2.22	226	0.44	1.77	0.12
7	1.96	3.7	2.19	37	2.46	1.90	0.12
8	2.57	2.8	2.17	85	1.82	1.44	0.09
9	2.62	2.7	2.76	50	2.05	0.80	0.09

<sup>a</sup>Units are  $10^{14}$  cm.<sup>b</sup>Units are  $10^{44}$  erg s $^{-1}$ .

TABLE A3  
OPTICAL CONTINUUM FLUXES AND X-RAY CONTINUUM PARAMETERS FROM THE 1998 GROUND-BASED/RXTE DATA.

epoch	JD–2450000	$F_{5100}^a$	1999 PCA responses <sup>b</sup>			2002 PCA responses <sup>c</sup>		
			$F_{210}^d$	$\Gamma^e$	$R^e$	$F_{210}^d$	$\Gamma^e$	$R^e$
1.0	979.96–980.40	$1.16 \pm 0.06$	8.0	$1.86 \pm 0.03$	$0.34^{+0.18}_{-0.18}$	7.9	$1.72 \pm 0.03$	$0.20^{+0.17}_{-0.13}$
2.1	985.09–985.40	$1.17 \pm 0.09$	7.8	$1.86 \pm 0.03$	$0.38^{+0.19}_{-0.17}$	7.7	$1.72 \pm 0.03$	$0.24^{+0.17}_{-0.14}$
2.2	985.69–986.41	$1.18 \pm 0.09$	9.8	$1.93 \pm 0.02$	$0.46 \pm 0.12$	9.5	$1.80 \pm 0.02$	$0.33^{+0.11}_{-0.10}$
2.3	986.65–987.40	$1.16 \pm 0.09$	9.5	$1.90^{+0.02}_{-0.01}$	$0.37^{+0.10}_{-0.04}$	9.3	$1.77^{+0.02}_{-0.03}$	$0.25^{+0.11}_{-0.10}$
2.4	987.63–987.86	$1.24 \pm 0.09$	9.1	$1.91^{+0.04}_{-0.03}$	$0.46^{+0.18}_{-0.13}$	8.8	$1.78^{+0.05}_{-0.04}$	$0.34^{+0.28}_{-0.20}$
3.1	994.36–994.89	$1.03 \pm 0.04$	6.9	$1.80^{+0.05}_{-0.04}$	$0.29^{+0.29}_{-0.14}$	6.8	$1.66^{+0.05}_{-0.04}$	$0.17^{+0.24}_{-0.17}$
3.2	995.64–996.13	$1.01 \pm 0.08$	5.6	$1.80^{+0.03}_{-0.02}$	$0.38^{+0.18}_{-0.09}$	5.5	$1.65^{+0.04}_{-0.03}$	$0.23^{+0.17}_{-0.14}$

<sup>a</sup>Units are  $10^{-14}$  erg cm $^{-2}$ s $^{-1}$ Å $^{-1}$ ; 1- $\sigma$  uncertainties.

<sup>b</sup>Using PCARSP V2.36 and PCARMF V3.5.

<sup>c</sup>Using PCARSP V8.0 and PCARMF V8.0.

<sup>d</sup>Units are  $10^{-11}$  erg cm $^2$ s $^{-1}$ .

<sup>e</sup>Uncertainties are computed for  $\Delta\chi^2 = 2.706$ .

TABLE A4

MODEL PARAMETERS FIT TO THE 1998 GROUND-BASED/RXTE DATA FOR  $r_{\min} = 2.4 \times 10^{14}$  CM AND  $r_{\min} = 3.2 \times 10^{14}$  CM (IN PARENTHESES). THESE PARAMETERS WERE DERIVED FROM SPECTRAL FITS THAT USED PCA RESPONSE MATRICES GENERATED BY PCARSP V2.36 AND PCARMF V3.5 (CHIANG ET AL. 2000).

epoch	$r_s$ ( $10^{14}$ cm)	$k_B T_e$ (keV)	$\tau$	$L_x^a$
1.0	3.78 (5.02)	554 (136)	0.09 (0.63)	5.15 (4.04)
2.1	3.79 (5.02)	684 (168)	0.06 (0.49)	5.21 (4.09)
2.2	4.64 (5.99)	27 ( 12)	2.26 (3.80)	4.28 (3.94)
2.3	4.24 (5.52)	89 ( 12)	0.90 (3.99)	4.57 (3.75)
2.4	4.38 (5.81)	204 ( 27)	0.36 (2.31)	4.92 (3.86)
3.1	3.24 (4.31)	676 (229)	0.07 (0.37)	5.00 (3.95)
3.2	3.24 (4.31)	1552 (526)	0.02 (0.11)	4.87 (3.84)

<sup>a</sup>Units are  $10^{44}$  erg s $^{-1}$ .

TABLE A5

MODEL PARAMETERS FIT TO THE 1998 GROUND-BASED/RXTE DATA FOR  $r_{\min} = 3.2 \times 10^{14}$  CM. THESE PARAMETERS WERE DERIVED FROM SPECTRAL FITS THAT USED PCA RESPONSE MATRICES GENERATED BY PCARSP V8.0 AND PCARMF V8.0.

epoch	$r_s$ ( $10^{14}$ cm)	$k_B T_e$ (keV)	$\tau$	$L_x^a$
1.0	3.72	346	0.25	5.57
2.1	3.72	393	0.21	5.63
2.2	4.34	135	0.69	4.85
2.3	4.07	164	0.59	5.05
2.4	4.16	305	0.26	5.48
3.1	3.43	285	0.38	5.05
3.2	3.39	471	0.19	4.98

<sup>a</sup>Units are  $10^{44}$  erg s $^{-1}$ .